Monthly Notices
of the
ROYAL ASTRONOMICAL SOCIETY

MNRAS **480,** 768–799 (2018)
Advance Access publication 2018 June 14

doi:10.1093/mnras/sty1553

Deep Extragalactic VIsible Legacy Survey (DEVILS): motivation, design, and target catalogue

L. J. M. Davies,[1★] A. S. G. Robotham,[1] S. P. Driver,[1] C. P. Lagos,[1,2] L. Cortese,[1] E. Mannering,[1,3] C. Foster,[4,5] C. Lidman,[6,7] A. Hashemizadeh,[1] S. Koushan,[1] S. O'Toole,[3] I. K. Baldry,[7] M. Bilicki,[8,9] J. Bland-Hawthorn,[4,5] M. N. Bremer,[10] M. J. I. Brown,[11] J. J. Bryant,[3,4] B. Catinella,[1] S. M. Croom,[4] M. W. Grootes,[12] B. W. Holwerda,[13] M. J. Jarvis,[14,15] N. Maddox,[16] M. Meyer,[1] A. J. Moffett,[17] S. Phillipps,[10] E. N. Taylor,[18] R. A. Windhorst[19] and C. Wolf[6]

Affiliations are listed at the end of the paper

Accepted 2018 June 7. Received 2018 June 3; in original form 2018 April 28

ABSTRACT

The Deep Extragalactic VIsible Legacy Survey (DEVILS) is a large spectroscopic campaign at the *Anglo-Australian Telescope* (AAT) aimed at bridging the near and distant Universe by producing the highest completeness survey of galaxies and groups at intermediate redshifts ($0.3 < z < 1.0$). Our sample consists of ∼60 000 galaxies to $Y < 21.2$ mag, over ∼6 deg^2 in three well-studied deep extragalactic fields (Cosmic Origins Survey field, COSMOS; Extended Chandra Deep Field South, ECDFS; and the X-ray Multi-Mirror Mission Large-Scale Structure region, XMM-LSS – all Large Synoptic Survey Telescope deep-drill fields). This paper presents the broad experimental design of DEVILS. Our target sample has been selected from deep Visible and Infrared Survey Telescope for Astronomy (VISTA) *Y*-band imaging (VISTA Deep Extragalactic Observations, VIDEO and UltraVISTA), with photometry measured by PROFOUND. Photometric star/galaxy separation is done on the basis of near-infrared colours and has been validated by visual inspection. To maximize our observing efficiency for faint targets, we employ a redshift feedback strategy, which continually updates our target lists, feeding back the results from the previous night's observations. We also present an overview of the initial spectroscopic observations undertaken in late 2017 and early 2018.

Key words: methods: observational – surveys – galaxies: evolution – galaxies: groups: general – galaxies: haloes – cosmological parameters.

1 INTRODUCTION

Over the past two decades, large low redshift ($z < 0.3$) galaxy evolution-focused surveys such as the Sloan Digital Sky Survey (SDSS, e.g. Abazajian et al. 2009), the Two Degree Field Galaxy Redshift Survey (2dFGRS, Colless et al. 2001), and Galaxy And Mass Assembly Survey (GAMA, Driver et al. 2011; Liske et al. 2015) have unequivocally changed our view of the local Universe. These surveys have parametrized structures on physical scales covering ∼5 orders of magnitude and characterized many of the astrophysical processes occurring at the current epoch. They have transformed our understanding of large-scale structure on scales of >1 Mpc (e.g. Peacock et al. 2001), the baryon-dark matter interface on scales of a few kpc to 1 Mpc (e.g. Yang et al. 2007; Robotham et al. 2011), the internal growth of galaxy structure of 1 to a few kpc scales (e.g. Lange et al. 2015; Belli, Newman & Ellis 2017), the low stellar mass Universe (e.g. Baldry et al. 2010), and the effect of both large-scale environment (e.g. Peng et al. 2010) and local environment (Patton et al. 2011; Davies et al. 2015b, 2016a) on galaxy evolution. However, by design these surveys have targeted only the relatively local Universe ($z < 0.3$). While they provide a wealth of information about galaxies at the current epoch, they cannot measure the astrophysical processes that led to their formation. It is not the processes occurring today that shaped the $z \sim 0$ Universe but the factors that drove galaxy evolution and structure formation over the preceding 10 billion years.

Deep but small-area spectroscopic surveys such as zCOSMOS-deep (Lilly et al. 2007), the Very Large Telescope (VLT) VIsible Multi-Object Spectrograph (VIMOS) Deep Survey (VVDS, Le

★ E-mail: luke.j.davies@uwa.edu.au

Fèvre et al. 2013), and VIMOS Ultra-Deep Survey (VUDS, Le Fèvre et al. 2015) have explored earlier epochs ($z > 1$), probing the initial stages of galaxy evolution. However, it is the relatively undersampled epoch at intermediate redshifts ($0.3 < z < 1.0$), where both galaxies and their host haloes undergo significant coeval evolution, specifically in terms of the environmental effects on galaxies. At this epoch, many of the $z \sim 0$ environmental trends observed in surveys such as GAMA and SDSS were shaped (e.g. Darvish et al. 2016). It is here that roughly half of all stars were formed (Madau & Dickinson 2014; Driver et al. 2018); galaxies underwent significant mass, size, morphology, and angular momentum evolution (e.g. Lotz et al. 2011; van der Wel et al. 2012; Codis, Pichon & Pogosyan 2015; Lange et al. 2015); and our current cold dark matter model ΛCDM predicts a strong and testable evolution of the halo mass function (e.g. Murray, Power & Robotham 2013; Elahi et al. 2018). Surprisingly, this key epoch in the formation of the fundamental relationships we observe today has been left comparatively unexplored.

To probe the processes that shaped the local Universe, we require a consistent parametrization of both galaxies and the larger scale dark matter distribution in which they reside. This can be achieved only through the identification of structures on sub-Mpc (group) scales. On these scales, dark matter haloes virialize and merge, and gas collapses to form galaxies. Thus, this regime is paramount to our understanding of baryon physics and the interplay between dark matter and directly observable galaxy components. To study sub-Mpc scales, spectroscopic completeness is key, as even the most high-fidelity photometric redshifts are not precise enough to identify these structures. However, at intermediate redshifts there is a paucity of fully sampled and complete spectroscopic surveys.

Until recently, the state-of-the-art survey that probed this epoch (zCOSMOS-bright, Lilly et al. 2007) was encumbered by its very small area ($\sim$1 deg^2), sparse sampling, and complex footprint (due to slit-mask spectroscopy). This ultimately leads to low completeness (only $\sim$50 per cent to $i < 22$; see Davies et al. 2015a). Other surveys at this epoch have focused on the sparse sampling of colour-selected populations over large volumes, such as the VIMOS Public Extragalactic Redshift Survey (VIPERS, Garilli et al. 2014) and DEEP2/3 (Cooper et al. 2012; Newman et al. 2013). More recently, the VLT's Large Early Galaxy Census (LEGA-C van der Wel et al. 2016) has focused on the sparse sampling of K-band-selected galaxies at $0.6 < z < 1.0$ but reaching high signal-to-noise continuum spectra for the detailed study the ages, metallicities, and velocity dispersions of galaxies at this epoch. The designs of these surveys, while matched to their specific science goals, are not tuned to studying the evolution of galaxy groups, mergers, sub-Mpc structure, and the influence of environment on galaxy evolution (see Figs 1 and 2). These are highly significant regimes that contribute to the formation of the fundamental relations observed today. To date, a holistic view of galaxy evolution over cosmic history relies on stitching together census-class surveys of the nearby Universe with these sparsely sampled pencil-beam surveys of the very distant Universe.

Recently, there have been a number of surveys that apply the high spectroscopic completeness approach to slightly fainter magnitudes than GAMA but in smaller area fields, such as the Active Galactic Nuclei (AGN) and Galaxy Evolution Survey (AGES, covering 7.7 deg^2 to $\sim$94 per cent completeness at $i < 20$ mag, Kochanek et al. 2012), the Smithsonian Hectospec Lensing Survey (SHELS, covering 8 deg^2 to $\sim$94 per cent completeness at $r < 20.2$ mag, Geller et al. 2016), and hCOSMOS (covering 1 deg^2 to >90 per cent completeness at $r < 20.6$ mag, Damjanov et al. 2018).

To continue this trend out to higher redshifts and to overcome the issues associated with sparely sampled surveys, we are undertaking the Deep Extragalactic VIsible Legacy Survey (DEVILS[1]) – a magnitude-limited ($Y < 21.2$ mag, $\sim$1.5 magnitudes fainter than AGES), high completeness (> 95 per cent) spectroscopic survey of three well-established legacy fields: XMM-Newton Large-Scale Structure field, XMM-LSS, Extended Chandra Deep Field-South, ECDFS, and Cosmological Evolution Survey field, COSMOS (see Fig. 3). DEVILS is designed to detect down to the stellar masses of $M^*_{z=0}$ galaxies to $z = 1$ ($10^{10.8}$ M$_\odot$ – the typical galaxy in the local Universe in terms of mass-density budget, Wright et al. 2017), major merger pairs of M$^*_{z=0}$ galaxies to $z = 0.8$, and groups down to 10^{13} M$_\odot$ to $z = 0.7$ (Fig. 2).

In this paper, we present the DEVILS survey design – including key science, field selection, and auxiliary data (Section 3), generation of the DEVILS target list – including source finding, masking, photometric separation of potential stars and galaxies and visual classification (Section 4), an overview of our final input catalogue and observing strategy (Section 5), and early results from the 2017/B observations (Section 6.4).

2 KEY SCIENCE OVERVIEW AND MOTIVATION

In this section, we describe the key science objectives of DEVILS in the context of target selection and survey strategy. While the legacy impact of DEVILS will be open-ended, here we highlight the two key science goals of the project. This section is designed to provide an introduction to the core DEVILS science and motivate the subsequent survey design.

2.1 The late-time evolution of the Halo Mass Function

The distribution of dark matter haloes (Halo Mass Function, HMF, e.g. Press & Schechter 1974; White & Rees 1978) and their evolution is one of the strongest predictions of the ΛCDM cosmological model. With the advent of precision cosmology from the Wilkinson Microwave Anisotropy Probe (WMAP, Bennett et al. 2013) and *Planck* (Planck Collaboration I, 2016), the theoretical prediction of the HMF and its evolution places a robust constraint on the distribution of matter at a given epoch. Combined, the ΛCDM model and concordance cosmology now predict the complete development of structures on >5 Mpc scales from the surface of last scattering (CMB, $z \sim 1100$), to the current epoch, with zero free parameters (on smaller scales, baryon physics is required to explain the growth of structure). Comparison of the HMF at $z < 0.1$ over three orders of magnitude (GAMA – Robotham et al., in preparation) demonstrates a remarkable affirmation of the $z = 0$ ΛCDM paradigm. The next critical challenge for ΛCDM is to test the predicted strong evolution of the HMF from $z = 1$ to $z = 0.1$. This evolution arises from the late-time assembly of clusters and massive groups (e.g. Vikhlinin et al. 2009).

One of the primary ways to directly parametrize dark matter to low halo masses (group scale) is through the construction of group catalogues (i.e. Yang et al. 2007; Robotham et al. 2011). Other approaches (CMB, redshift space distortions, strong/weak lensing, X-ray luminosities) can statistically recover the total dark matter content and provide some information of its distribution but cannot recover individual halo masses except for the most massive, and

[1] https://devilsurvey.org/

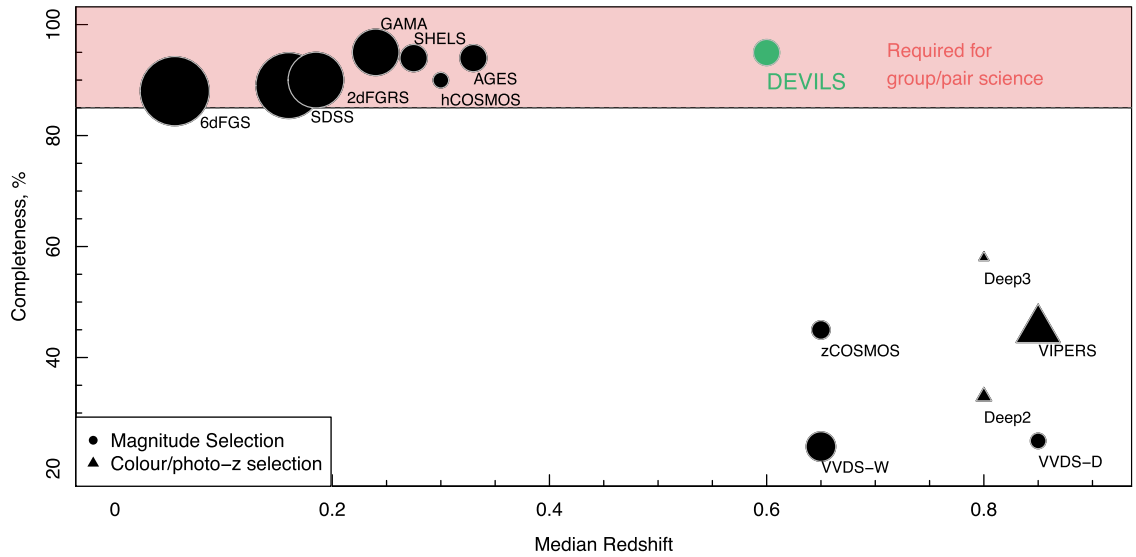

Figure 1. DEVILS comparison to other existing large spectroscopic surveys in terms of completeness and median redshift of the target sample. Surveys are split by those that use a simple single-band selection function (circle) and those that use a more complex colour and/or photometric redshift selection (triangles). Point size is representative of log10[number of sources]. In order to explore the effect of sub-Mpc structure on the evolution of galaxies and to probe the evolution of group-scale haloes, high completeness to magnitude-limited samples are required. Surveys with a completeness of $\lesssim$85 per cent miss a significant fraction of group galaxies and therefore can only parametrize the most massive haloes (see Section 3.2 and Fig. 2), and are also very incomplete to interacting pairs. For example, with uniform random sampling, to zeroth order, a survey that is 50 per cent complete at a given stellar mass will identify only 25 per cent of major merger pairs at that mass, while a similar 95 per cent complete sample will identify 90 per cent of pairs. Low redshift surveys, such as SDSS, 2dFGRS, and GAMA, probe to these high levels of completeness in the relatively local Universe. However, until DEVILS, there has been no survey undertaken with this level of completeness at intermediate redshift.

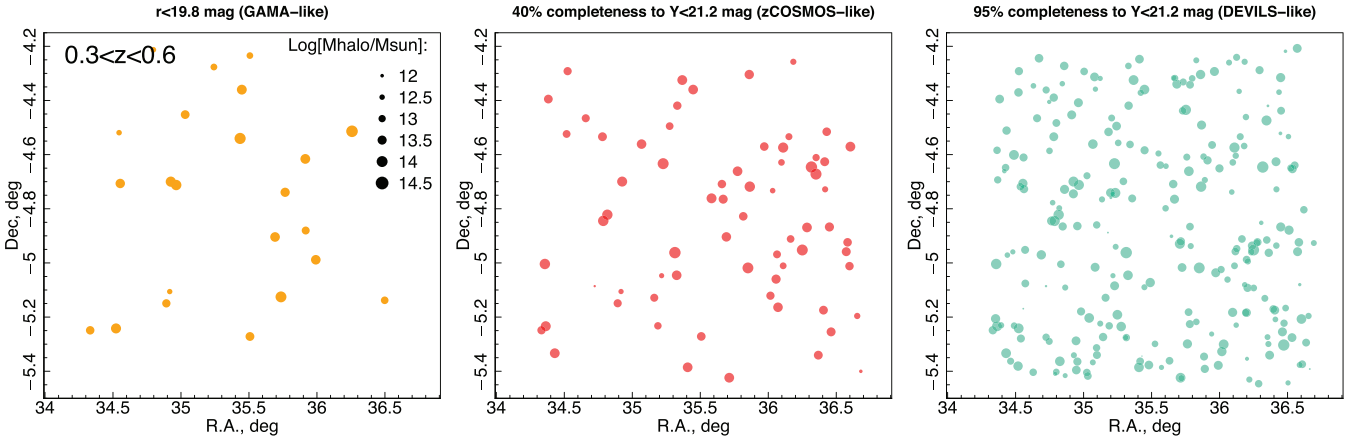

Figure 2. The predicted distribution of multiplicity $N > 3$ haloes identifiable in the D02 region for our DEVILS Theoretical Astrophysical Observatory (TAO) simulations (see Section 3.2). The size of the point represents halo mass on a log scale given in the legend. Left: Distribution of haloes that would be identified at $.3 < z < 0.6$ using a GAMA-like $r < 19.8$ limit. Middle: Distribution of haloes that would be identified at $0.3 < z < 0.6$ using a DEVILS-like $Y < 21.2$ mag limit but with only 40 per cent completeness (comparable to other surveys at this epoch, such as zCOSMOS-bight and VIPERS). We assume uniform incompleteness and remove 60 per cent of $Y < 21.2$ mag galaxies. Right: Distribution of haloes that would be identified at $0.3 < z < 0.6$ using a DEVILS-like $Y < 21.2$ mag limit and with 95 per cent completeness limit, highlighting that low completeness surveys miss a large fraction of low-mass haloes.

rare, clusters. However, through groups we can parametrize the dark matter mass (and average density) of individual haloes down to $\sim 10^{12}$ M$_\odot$, as the group member's motions directly map to halo mass ($M_{halo} \propto \sigma^2 r$ or r^3, Eke et al. 2006; Robotham et al. 2011, with typical errors in halo mass of ∼0.7dex for low multiplicity groups, $N = 4$–5). At this limit, approximately 30 per cent of the dark matter is bound (and hence constrained, Robotham et al., in preparation), with the remainder either entirely unbound or in lower mass haloes. Nevertheless, group catalogues provide an extremely powerful mechanism to directly uncover a considerable fraction of the underlying dark matter *distribution* within a specific volume by tracing out the gravitational potential defined by filamentary structure (e.g. Alpaslan et al. 2014; Darvish et al. 2015; Viola et al. 2015; Kraljic et al. 2018).

GAMA has led the way in constraining the distribution of haloes to low masses in the local Universe ($M_{Halo} \sim 10^{12}$ M$_\odot$ at $z < 0.2$,

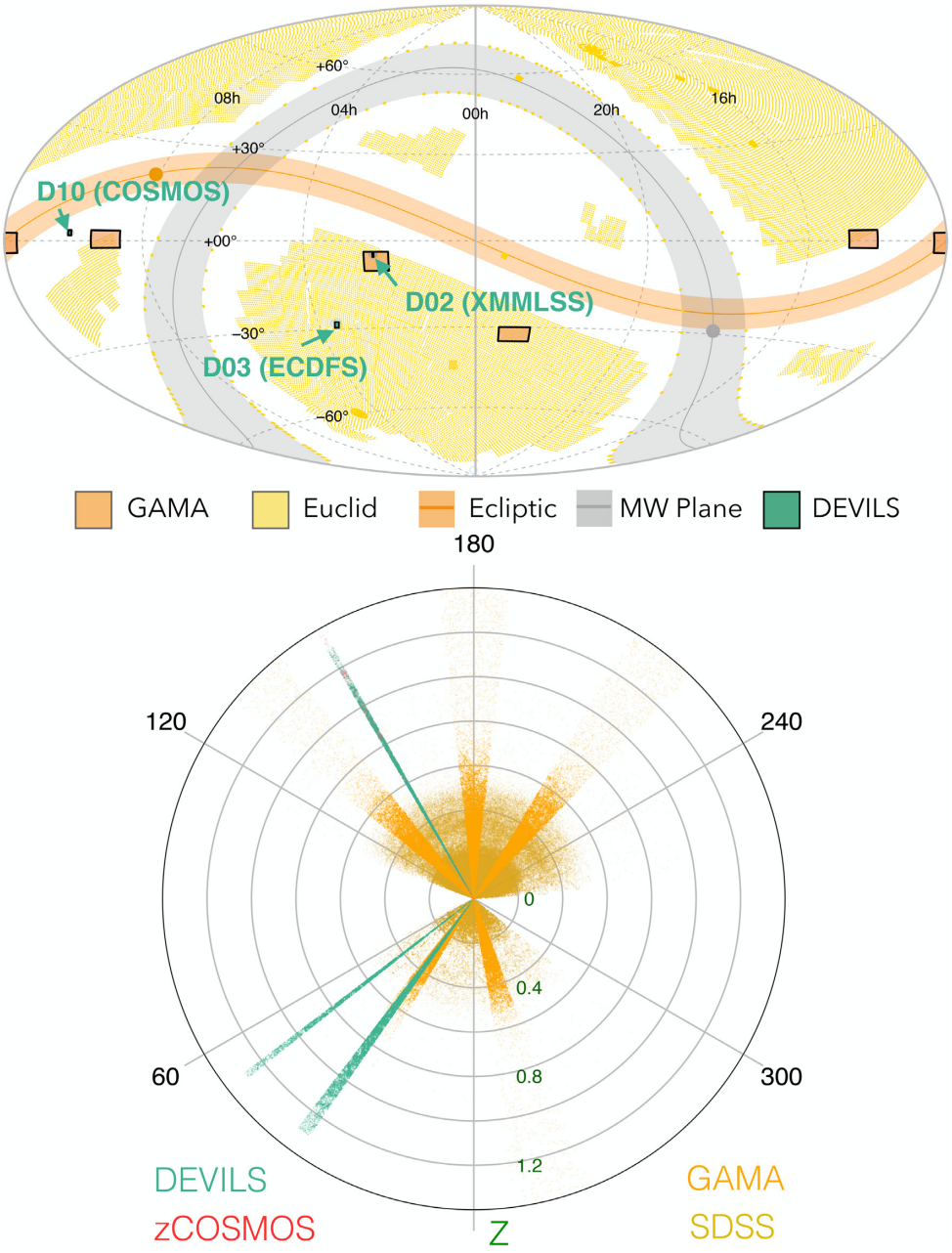

Figure 3. DEVILS field positions with respect to the GAMA regions and current Euclid footprint (top) produced by ASTROMAP (astromap.icrar.org) and predicted light cones distribution of DEVILS sources from our Theoretical Astrophysical Observatory (TAO) simulations (see Section 3.2) in comparison to SDSS, GAMA, and zCOSMOS (note zCOSMOS sits under the D10 distribution at ∼150 deg but extends to slightly higher redshift).

Robotham et al. 2011). Observationally, however, we know little about the evolution of group-scale haloes at higher redshifts and have previously been restricted by the use of photometric redshifts (e.g. Leauthaud et al. 2012; Hatfield et al. 2016). By conducting a survey specifically optimized for the identification of group-scale dark matter haloes to $z = 0.7$ (see Fig. 2), DEVILS will confirm the evolution, or lack thereof, in the massive-end of the HMF, extending below the massive cluster regime probed by X-ray cluster surveys (e.g. Vikhlinin et al. 2009). This will provide a stringent test of one of the clearest predictions of ΛCDM (Fig. 4). In addition, recently proposed alternative approaches to identify ΛCDM tension using cluster/group velocity dispersions alone (Caldwell et al. 2016) can be directly tested via the construction of group catalogues in deep spectroscopic surveys (such as DEVILS).

2.2 The effect of environment in regulating galaxy evolution over the last 8 Gyr

One of the most fundamental questions in astrophysics is what processes have shaped the formation and evolution of galaxies we observe today? To answer this question, we typically use two complementary methods: either probing the factors that affect the growth of individual galaxies as a function of stellar mass, environment, epoch, etc., or by measuring the global evolution of the ensemble

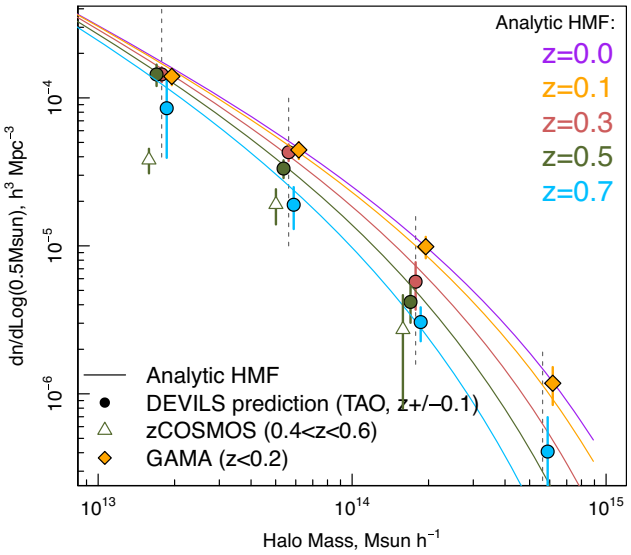

Figure 4. Evolution of the analytical form of the halo mass function (HMF) from ΛCDM and DEVILS observational predictions from our Theoretical Astrophysical Observatory (TAO) simulations (see Section 3.2). Solid lines display the analytic form of the HMF from Murray et al. (2013) at a range of redshifts. We assume that a dark matter halo has its mass parametrized if we detect >3 group members at our $Y < 21.2$ mag limit and show the resultant predicted DEVILS HMF at each epoch. We also display the HMF measured using the zCOSMOS groups sample of Knobel et al. (2012) at $0.4 < z < 0.6$. If present, DEVILS will measure the late-time evolution of the high-mass end of the HMF predicted by ΛCDM.

galaxy population via distributions such as the stellar mass function (SMF, e.g. see Marchesini et al. 2009; Behroozi, Wechsler & Conroy 2013; Muzzin et al. 2013; Tomczak et al. 2014; Driver et al. 2018) or cosmic star-formation history (e.g. see Bell et al. 2005; Hopkins & Beacom 2006; Schaye et al. 2010; Madau & Dickinson 2014; Davies et al. 2016b; Driver et al. 2018). It is the former of these methods which ultimately probes the processes that shape the latter. As such, we would ideally like to target both the underlying astrophysics *and* the fundamental relations which they produce. To date, we have exquisitely probed these global relations in the local Universe (e.g. Bell et al. 2003; Panter, Heavens & Jimenez 2004; Elbaz et al. 2007; Peng et al. 2010; Baldry et al. 2012; Chang et al. 2015; Moffett et al. 2016; Davies et al. 2016b; Wright et al. 2017) and also have some understanding of how the distributions vary with time (e.g. Behroozi et al. 2013; Vulcani et al. 2013; Madau & Dickinson 2014; Lee et al. 2015) and environment (e.g. Yang, Mo & van den Bosch 2009; Bolzonella et al. 2010; McNaught-Roberts et al. 2014; Eardley et al. 2015; Davidzon et al. 2016; Tomczak et al. 2017). However, the astrophysics involved in *shaping* these distributions at each epoch/environment are far from clear.

Measuring the factors that govern the growth of galaxies is problematic. Most simplistically, there are two high-level mechanisms that shape the UV-FIR properties by which we trace galaxy evolution: star formation (SF, e.g. see review of Kennicutt & Evans 2012) and mergers (e.g. Bundy et al. 2004; Baugh 2006; Kartaltepe et al. 2007; Bundy et al. 2009; de Ravel et al. 2009; Jogee et al. 2009; Lotz et al. 2011; Robotham et al. 2014, and see review of Conselice 2014), which, respectively, form and redistribute the stellar material. However, a complex array of effects all have a significant impact on the evolution of galaxies, such as black hole growth (Hopkins et al. 2008; Kormendy & Ho 2013), AGN feedback (Kauffmann et al. 2004; Fabian 2012), gas accretion (Kauffmann et al. 2006; Sancisi et al. 2008), starvation/strangulation (Moore et al. 1999), atomic-to-molecular gas fraction (e.g. Wong & Blitz 2002; Bigiel et al. 2008; Popping, Somerville & Trager 2014), tidal stripping (Gunn & Gott 1972; Moore et al. 1999; Brown et al. 2017; Poggianti et al. 2017), harassment (Larson, Tinsley & Caldwell 1980), morphological transformations (Conselice 2014; Eales et al. 2015), and very local (Patton et al. 2011; Scudder et al. 2012, 2015; Davies et al. 2015b) and larger scale (Dressler 1980; Giovanelli & Haynes 1985; Peng et al. 2010; Cortese et al. 2011; Darvish et al. 2016) environments. All of these factors largely drive the observed changes to star formation and merger state. It is the varying contribution of these processes over the history of the Universe that leads to the relations we observe today.

2.2.1 *Star formation, mergers, and the growth of stellar mass*

In the local Universe, we have begun to explore how mergers and star formation are changing the distribution of stellar material at the current epoch. Robotham et al. (2014) determined robust merger rates for GAMA and estimated the relative contribution of *in situ* star formation and mergers in shaping the $z \sim 0$ SMF. They found that $M^*_{z=0}$ represents an important transition between merger- and SF-dominated growth, with sub-$M^*_{z=0}$ galaxies predominantly growing via star-formation and larger mass galaxies gaining their mass via mergers. However, we know very little about how these relative contributions evolve with redshift. For example, we know that both star formation and merger rates increase with look-back time (e.g. Lotz et al. 2011; Lee et al. 2015), but does the relative stellar mass growth via these mechanisms evolve consistently? And can their relative contribution account for the evolution in the shape of the SMF? Interestingly, Bell et al. (2003) find that while the majority of stars formed at $z < 1$ are produced in blue late-type galaxies, the bulk of stellar mass is accumulated in red early-type galaxies, suggesting that it is both star formation and mergers at intermediate redshift that contribute strongly to formation of the observed $z \sim 0$ mass function.

To investigate these processes requires, at least, measurements of both star formation and mergers over a broad redshift range and to a much higher velocity resolution than obtainable by photo-zs alone ($<100\,\mathrm{km\,s^{-1}}$ compared to $\sim 1000\,\mathrm{km\,s^{-1}}$ for photo-zs). Previously, a number of surveys have explored the interplay between star formation and mergers at intermediate redshift, using precise photo-zs and high-resolution imaging. Most notable of these is the Galaxy Evolution from Morphologies and SEDs (GEMS) survey (Rix et al. 2004), which combined deep *Hubble Space Telescope* (*HST*) imaging with the precise ($\delta z/(1+z) = 0.006 \pm 0.020$) photo-$z$s of the Classifying Objects by Medium-Band Observations in 17 Filters survey (COMBO17, Wolf et al. 2001, 2004). The GEMS+COMBO17 survey provides invaluable information about the contribution of ongoing major mergers at intermediate redshifts (e.g. Bell et al. 2006; Robaina et al. 2009), i.e. those identified via visual disturbance in *HST* imaging. However, without spectroscopic redshifts to identify close, but not visually disturbed, pair systems they may be missing a significant fraction of merger events. In addition, the lack of environmental resolution (i.e. to the group scale) provided by photo-zs inhibits these surveys from exploring the environmental trends of mergers and star-formation activity.

Simulations add little constraint to merger rates with models predicting half an order of magnitude variation of different merger types: i.e. major/minor – defined at a 3:1 stellar mass ratio, and

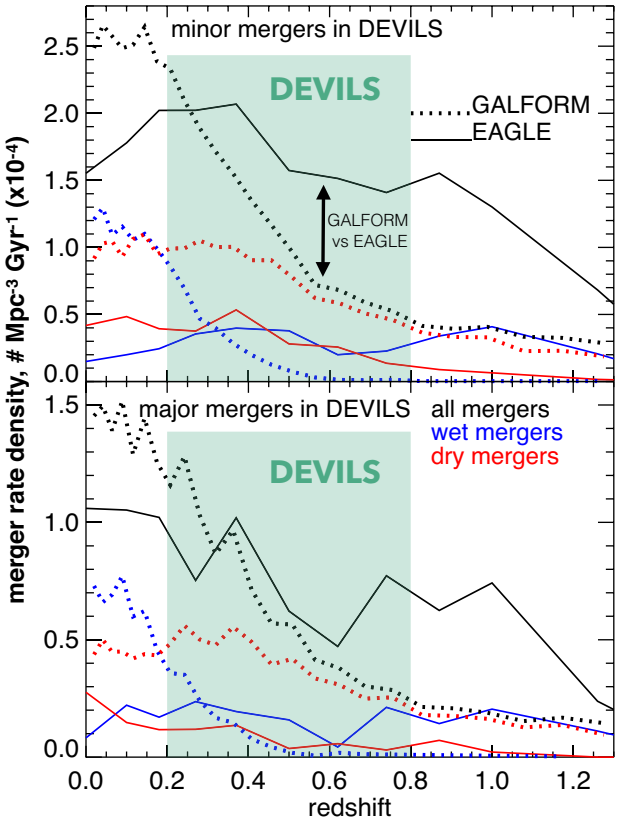

Figure 5. GALFORM (dotted lines) and EAGLE (solid lines) predictions for minor (top)/major (bottom) and wet (blue)/dry (red) merger rates at a DEVILS-like stellar mass limit. Here wet/dry mergers are defined by hydrogen gas content with $(M_{\rm H1}+M_{\rm H2})/M_{\rm star} > 0.5$ and <0.1 for wet and dry, respectively (i.e. intermediate gas fractions are not displayed). Over the DEVILS volume, GALFORM and EAGLE predict very different major–minor merger rates (factor of 2) and major wet–dry merger fractions (factor of $\sim$10).

wet/dry – based on HI gas content. Thus, to constrain these models further, we require stronger observational constraints. For example, at a DEVILS-like stellar mass limit, the Evolution and Assembly of GaLaxies and their Environments (EAGLE; Schaye et al. 2015) and Galform (Lacey et al. 2016) models predict vastly different minor merger rates and wet/dry merger fractions at $z > 0.3$ (Fig. 5 and see Lagos et al. 2018, for an example of mergers in EAGLE).

To differentiate between the effect of interactions in competing galaxy formation models, we must robustly identify highly complete samples of merging galaxies at intermediate redshift. Within DEVILS, we will have a sample with which to identify pre-merger pairs (as in Robotham et al. 2014), deep high-resolution imaging to identify post-merger systems, and complementary HI data to explore the importance of wet/dry mergers (see Section 3.3). Combined this will allow us to explore the relative contribution of star-formation and mergers in shaping the local galaxy population.

2.2.2 The environmental dependence of galaxy evolution

Observationally, it has long been known that in the local Universe the cluster environment on scales of >1 Mpc can leave strong imprints on galaxies. These environments can affect properties such as morphology (Dressler 1980), colour (Kodama et al. 2001), stellar mass (Ostriker & Tremaine 1975), AGN fraction (Kauffmann et al. 2004), star formation (Peng et al. 2010), gas content (Gunn & Gott 1972), and kinematic structure (e.g. Cappellari et al. 2011; Fogarty et al. 2014). More recently, within GAMA and SDSS, we have begun to explore the effect of more local environment ($<$ Mpc, groups & pairs). Numerous studies have found that while different environments can display different luminosity/mass functions, when controlled for mass, it is local galaxy–galaxy interactions that leave the strongest imprint on galaxy properties (e.g. Alpaslan et al. 2015; Scudder et al. 2015; Grootes et al. 2017). Specifically, the effect of $<$ Mpc environment can drive significant (factor of $\sim$4) changes to star formation (e.g. Patton et al. 2011; Scudder et al. 2012; Davies et al. 2015b, 2016a). These changes are intimately linked to the underlying atomic and molecular gas distribution, which can be easily disrupted in overdense environments via turbulence, ram-pressure stripping, and strangulation (i.e. Nichols & Bland-Hawthorn 2011, 2013).

At higher redshifts, the quiescent fraction in overdense environments is found to evolve dramatically to $z \sim 1$ (Darvish et al. 2016) and potentially even reverse at $z > 1$ (Elbaz et al. 2007). However, more recent results from *Herschel* suggest that this reversal may occur at much earlier times (for example, see Elbaz et al. 2007; Popesso et al. 2011, 2012; Ziparo et al. 2014). In terms of structure, the morphology–density relation in the most massive clusters appears in place by $z \sim 1$ but in group-sized haloes evolves dramatically between $0 < z < 1$ (Smith et al. 2005). In addition, determining the relative importance of large-scale astrophysical processes such as pre-processing in group environments at these redshifts is essential in understanding the observed environmental trends at $z \sim 0$.

DEVILS will simultaneously trace the evolution of galaxies *and* structure on 0.01–10 Mpc scales ranging from mergers and pairs to groups, clusters, filaments, and voids. This will allow us to finely grid in stellar mass, morphology, halo mass, environment, and epoch (see Section 3) to determine the origin of the $z \sim 0$ fundamental relations observed by GAMA and SDSS.

3 SURVEY DESIGN

3.1 Facility and instrument characteristics

DEVILS spectroscopic observations are currently being undertaken at the 3.9m *Anglo-Australian Telescope* at the Siding Spring Observatory in New South Wales with the AAOmega fibre-fed spectrograph (Saunders et al. 2004; Sharp et al. 2006) in conjunction with the Two-degree Field (2dF, Lewis et al. 2002) positioner. The 2dF positioner has been at the forefront of large galaxy redshift surveys in the local Universe (such as 2dFGRS and GAMA) and has also been used to great success in targeting large numbers of sources to higher redshift (e.g. 2dFLenS and WiggleZ, Blake et al. 2016; Drinkwater et al. 2018) and more recently to faint magnitudes (OzDES, Childress et al. 2017). As such, it is an ideal facility to perform our deep intermediate redshift survey. 2dF allows the simultaneous observation of $\sim$400 targets with the AAOmega spectrograph, with 2″ diameter fibres. The 2dF top-end consists of an atmospheric dispersion compensator and robot gantry that positions fibres to 0.3″ accuracy on sky.

AAOmega observes in two spectral channels (blue and red), both equipped with a 2k $\times$ 4k E2V CCD detector and an AAO2 CCD controller. We observe with the 5700 Å dichroic allowing for simultaneous coverage from 3750 Å to 8850 Å. For the blue CCD, we use the 580V grating with central wavelength of 4820 Å providing a $\sim$1.03 Å/pix dispersion, while for the red CCD, we use the 385R

gating with central wavelength of 7250 Å providing a ∼1.56 Å/pix dispersion. This results in a spectral resolution that varies from $R \sim 1000$ (blue) to $R \sim 1600$ (red). This spectral resolution and wavelength range was selected to enable detection of at least the [OII] (3727 Å) emission line and 4000 Å break over our full target redshift range and provide sufficient velocity resolution with which to identify close pairs (<50 km sec^{-1}; see Robotham et al. 2014).

3.2 Selection band, depth, and area

3.2.1 DEVILS simulations using the TAO tool

In the following subsections, we describe how we define the DEVILS selection band, depth, and area. This is largely achieved using simulated DEVILS light cones generated using the TAO (Bernyk et al. 2016) tool.[2] Here we briefly describe the TAO simulations we generate and any assumptions made. Note that TAO provides all of the functionality to go from these input parameters to fully simulated light cones.

We use Millennium *N*-body simulation with WMAP cosmology (Springel et al. 2005) coupled with the Semi-Analytic Galaxy Evolution (SAGE) model (Croton et al. 2016) to simulate the galaxy distribution in each of the DEVILS regions independently. When generating light cones, we restrict our simulated galaxies to $z < 1.2$ to limit computational time (the small number galaxies detected at $z > 1.2$ will be negligible in the DEVILS sample). Spectral energy distribution (SED) models from Bruzual & Charlot (2003) with a Chabrier initial mass function (Chabrier 2003) are used to estimate intrinsic galaxy magnitudes from the SAGE ages, starfromation histories (SFHs), and metallicities. Using the relationship between colour excess, E(B–V), and instantaneous star-formation rate, TAO estimates the dust content of each galaxy. The galaxy SED is then extincted using a Calzetti extinction law (Calzetti, Kinney & Storchi-Bergmann 1994) and observed-frame apparent magnitudes are calculated using the galaxy's luminosity distance, extincted SED, and common filter sets. TAO provides magnitude measurements for the Visible and Infrared Survey Telescope for Astronomy (VISTA) *Y* band, which we use for our DEVILS selection. All light cones are then cut at $Y < 22.0$ mag to limit computational time.

3.2.2 Selection band

To achieve the science goals stated previously, DEVILS must probe to faint magnitudes and high completeness and obtain robust samples of individual galaxies, pairs of galaxies, and groups. The majority of the galaxy evolution science we are undertaking in DEVILS requires stellar mass-selected samples (for example, see Taylor et al. 2011, and many other GAMA papers for a detailed discussion of the benefits of a stellar mass-based selection[3]). In addition, for our halo science, we require a relatively unbiased tracer of galaxies within haloes. As such, we would ideally like our target selection to be in terms of stellar mass. However, without prior distance information this cannot be achieved. Thus, we select based on a single imaging band that is closely correlated with stellar mass. While colours could be used, these create complex selection functions that can bias any galaxy evolution studies and may lead to biases in halo identification, as environment is a strong driver of galaxy colour (e.g. Kodama et al. 2001). Various authors (e.g. Bell & de Jong 2000; Taylor et al. 2011) have shown that the individual near-infrared (NIR) bands are most correlated with stellar mass, as they are dominated by emission from old stars (which in turn dominates the mass of the galaxy).

The most significant gains in directly relating a single observation band to stellar mass come from ensuring that the survey selection band remains above the 4000 Å break in the rest frame of the galaxy for the entire sample. This is true for all NIR bands to $z \sim 1$. Secondly, we also wish to stay as close as possible to the spectral observing range of the AAT+AAOmega, such that our selection band is representative of the spectral emission we will receive. Lastly, we also wish to select in a band that has consistent deep imaging, from the same facility/instrument over a number of deep fields spread in right ascension (see Section 3.3). We find that the VISTA *Y* band (centred at 1.02μm) uniquely meets all of these criteria.

3.2.3 Depth

The key science goals of DEVILS require us to trace the evolution of galaxies, galaxy interactions, and the most massive groups and clusters out to intermediate redshifts. In order to parametrize these, we aim to select galaxies to: (i) measure the evolution of typical $M^*_{z\sim0}$-like galaxies out to $z \sim 1$, (ii) identify all major merger (<3:1 mass ratio) pairs to $M^*_{z\sim0}$-like galaxies out to $z \sim 0.8$, and (iii) measure the mass of 10^{13} M$_\odot$ haloes out to $z \sim 0.7$. To test the depth required to achieve these goals, we use our simulated DEVILS survey volumes from TAO. We apply varying *Y*-band magnitude limits (between $20.0 < Y < 22.0$ mag) and investigate the resultant DEVILS sample we would obtain if we reached 95 per cent spectroscopic completeness (we randomly remove 5 per cent of sources, but note that in practice this will not be random but related to some galaxy characteristic). In terms of haloes, we assume that a dark matter halo has its mass measured if we detect more than three group members (with ∼0.7 dex error; Robotham et al. 2011). We find that to reach our target goals in terms of galaxies and haloes outlined above requires a Y <21.2 mag selection (and see Fig. 2). The resulting predicted stellar mass and halo mass distributions as a function of redshift are shown in Fig. 6. In the left-hand panel, we also highlight $M^*_{z\sim0}$ at $10^{10.8}$ M$_\odot$ (Wright et al. 2017) and the region where major merger pairs to $M^*_{z\sim0}$ galaxies (based on a 3:1 mass ratio) would be found – highlighting that we can detect both galaxies in these types of merger systems to $z \sim 0.7$. We then compare these to the distribution from GAMA (at low redshift, Liske et al. 2015) and zCOSMOS-bright (as a comparable sample at a similar redshift to DEVILS; Lilly et al. 2007). For groups we also show the 2dFGRS-2PIGG (Eke et al. 2006) distribution as a $z \sim 0$ and the ultimate XMM extragalactic survey (XXL) 100 bright cluster sample (Pacaud et al. 2016) to $z \sim 1$ for comparison.

3.2.4 Area

Using our TAO simulations, we can also make a simplistic estimation regarding the sample size we require to subdivide our population based on stellar mass, halo mass, and redshift in order to achieve our key science goals. To measure the evolution in the HMF, at a minimum we require ∼2/3 $z > 0.3$ redshift bins each containing a few tens of groups over a ∼0.5 dex range in halo mass. This will allow us to differentiate between the HMF at each epoch, assuming the analytic form predicted by ΛCDM to be correct, i.e.

[2] https://tao.asvo.org.au/tao/
[3] http://www.gama-survey.org/pubs/onads.php

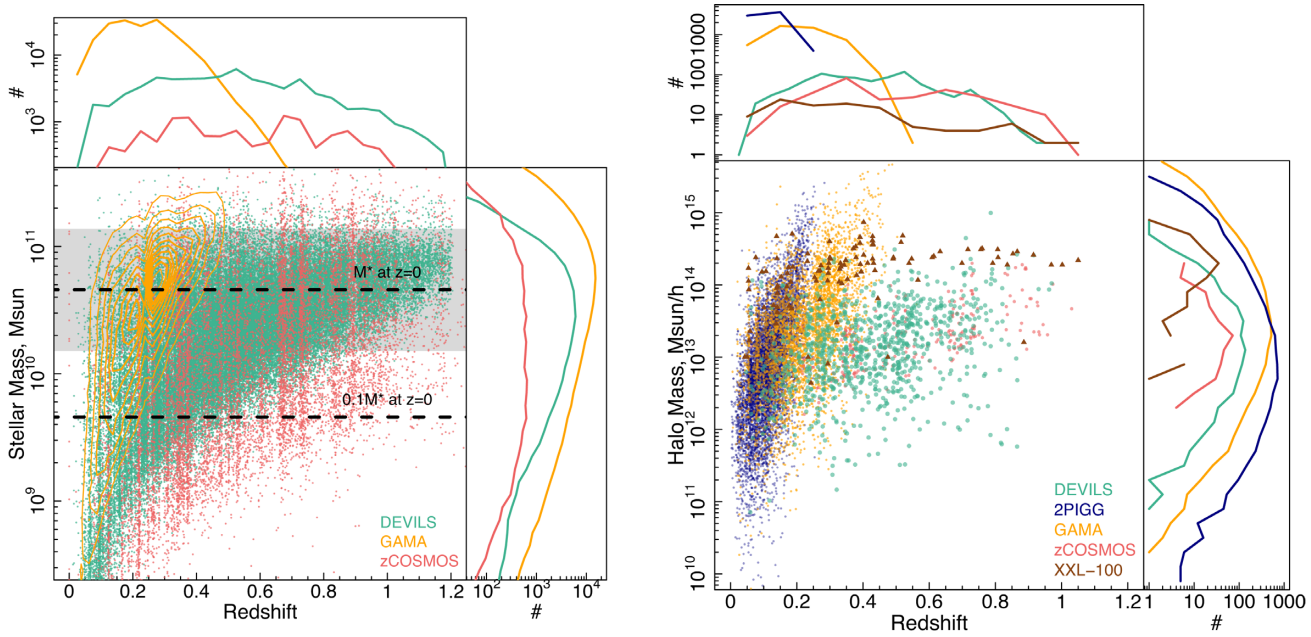

Figure 6. DEVILS predicted stellar mass-redshift distribution (left) and halo mass-redshift distribution (right). For clarity, in the left-hand hand panel, we show only density contours for the GAMA sample. Distributions are predicted using the Theoretic Astrophysical Observatory (TAO) for 6 deg^2, a $Y < 21.2$ mag selection and 95 per cent completeness (we randomly remove 5 per cent of sources). For group halo masses, we assume that a group with more than three members has its mass constrained. For comparison, we show the same distributions for both GAMA and zCOSMOS (and for groups 2dFGRS-2PIGG and the XXL-100 bright cluster sample). DEVILS will detect $M^*_{z\sim0}$ galaxies out to $z \sim 1$ (dashed line on the left-hand panel), identify major merger (<3:1 mass ratio) pairs to $M^*_{z\sim0}$ galaxies out to $z \sim 0.8$ (grey-shaded band on left-hand panel), and parametrize 10^{13} $M_\odot$ haloes out to $z \sim 0.7$ (right-hand panel).

in our TAO simulations with a few tens of groups in each 0.5 dex range, the combined errors on the measured HMF at $z = 0.3$ and $z = 0.7$ are smaller than the evolution in the analytic form of the HMF over this epoch (see Fig. 4). To constrain the SMF to $M^*_{z\sim0}$ at the high redshift end of our sample requires $\sim$1500 galaxies per $\Delta z = 0.2$ at $z = 0.8$–1 (much more at lower z). We note that these estimations are based on relatively simplistic assumptions, and are conservative, such that we should achieve our science goals. To reach these numbers in our TAO simulations, we require a sample size of $\gtrsim$50 000 galaxies to $Y < 21.2$ mag. Taking the deep NIR number counts of Driver et al. (2016a), we predict that to observe a sample of this size requires a target area $\sim$6 deg^2.

3.3 Field selection and existing data

In order to maximize the scientific return of the DEVILS project, we aim to target well-studied fields with extensive multiwavelength imaging and spectroscopy, which will also be targeted with upcoming next-generation facilities. First, this will allow for a detailed parametrization of the photometrically derived properties for DEVILS sources, and secondly, this will add lasting legacy to the DEVILS data set. There are a number of such fields that are accessible to the AAT. We select three of the most well-studied regions for our spectroscopic follow-up: the X-ray Multi-Mirror Mission Large-Scale Structure region (XMM-LSS, e.g. see Pierre et al. 2004), the Extended Chandra Deep Field-South region (ECDFS, see Virani et al. 2006), and Cosmic Evolution Survey region (COSMOS, Scoville et al. 2007). Our priority condition for the selection of these fields is consistent deep Y-band imaging to produce our target selection covering >6 deg^2. Each of these fields has deep VISTA imaging in the Y band (XMM-LSS/ECDFS – VIDEO, and COSMOS – UltraVISTA), which covers a total area of $\sim$10.5 deg^2. DEVILS field positions and areas are presented in Table 1. From this point on we shall refer to the DEVILS 2h field (XMM-LSS) as D02, the 3h field (ECDFS) as D03, and 10h field (COSMOS) as D10.

These three deep fields have also been targeted extensively with many multiwavelength imaging and spectroscopic programs that are essential to the DEVILS survey. Deep imaging data will be used for SED fitting and the determination of galaxy properties (see Andrews et al. 2017, for similar work in COSMOS), while existing spectra will be used within the DEVILS sample to maximize the scientific return of tehe program while minimizing observational costs (see Section 5.1.1).

In this paper, we briefly outline the previous key imaging and spectroscopic programs in the DEVILS regions and use in our target selection. A more detailed analysis of the DEVILS multiwavelength data and derived products will be presented in later work. We highlight that all three fields contain deep X-ray (Pierre et al. 2006; Cappelluti et al. 2009; Ranalli et al. 2013; Chen et al. 2018), UV (Xu et al. 2005; Zamojski et al. 2007), optical (de Jong et al. 2013; Taniguchi et al. 2015; Vaccari et al. 2016; Aihara et al. 2017), NIR (McCracken et al. 2012; Jarvis et al. 2013), MIR (Lonsdale et al. 2003; Surace et al. 2004; Sanders et al. 2007; Mauduit et al. 2012; Lin et al. 2016), FIR (Oliver et al. 2012), and radio continuum (Norris et al. 2006; Tasse et al. 2006, 2007; Schinnerer et al. 2007; Aretxaga et al. 2011; Huynh et al. 2012; Miller et al. 2013; Smolčić et al. 2014, 2017; Hale et al. in preparation) imaging. It is also worth noting that the deep X-ray data in these fields will provide complementary X-ray-derived group/cluster masses for the DEVILS sample, providing an independent test of our derived masses, and

Table 1. DEVILS field positions, areas, and target selection imaging.

Field	Common Name	RA,Dec (cen) (sex)	RA,Dec (cen) (deg)	RA,Dec (min) (deg)	RA,Dec (max) (deg)	Area (deg)	Band	Depth (mag)	Survey	Limit (5σ AB)
D02	XMM-LSS	02:22:06.0, −04:42:00.0	35.53, −4.70	34.00, −5.20	37.05, −4.20	3.00	VISTA-*Y*	21.2	VIDEO	25.0
D03	ECDFS	03:32:27.12, −28:00:00.0	53.113, −28.00	52.263, −28.50	53.963, −27.50	1.50	VISTA-*Y*	21.2	VIDEO	24.9
D10	COSMOS	10:00:09.6, 02:13:12.0	150.04, 2.22	149.38, 1.65	150.70, 2.79	1.50	VISTA-*Y*	21.2	UltraVISTA	>24.8

allowing a detailed exploration of the comparison between spectroscopically derived group properties and those determined via X-ray emission. This will be explored further when the DEVILS sample is complete.

These fields are also of strong interest for ongoing/upcoming large observational programs. Subaru-Hyper Suprime Camera (Aihara et al. 2017) is currently undertaking deep imaging programs over the DEVILS fields (e.g. see Tanaka et al. 2017, in D10) and all three regions have been announced as Large Synoptic Survey Telescope (LSST) deep-drill fields (see Gawiser et al - LSST white paper[4]). Euclid (Laureijs et al. 2011) and the Wide Field Infrared Survey Telescope will provide high-resolution imaging in D02/D03 to complement the existing *HST* imaging in D10, and MeerKAT International GHz Tiered Extragalactic Exploration (MIGHTEE, Jarvis et al. 2017) will produce deep 1.4-GHz observations in all three fields to supplement existing Very Large Array (VLA) continuum observations in D10 (Schinnerer et al. 2007; Smolčić et al. 2014, 2017).

Finally, these fields are also the location of the next-generation deep HI surveys. The Jansky VLA's Cosmic HI Large Extragalactic Survey (CHILES, Fernández et al. 2013) is currently ongoing in D10 and will probe 21-cm emission from galaxies to $z < 0.45$, while MeerKAT programs MIGHTEE-HI in all three fields, and Looking At the Distant Universe with the MeerKAT Array (LADUMA, Holwerda et al. 2011) in D03 will target HI to $z \sim 0.58$ and $z \sim 1.4$, respectively. Combined, MIGHTEE-HI and LADUMA will cover the full DEVILS area. The combination of the DEVILS sample with these HI surveys is a tantalizing prospect both in terms of stacking DEVILS sources to extend further down the HI mass function (Lah et al. 2007; Verheijen et al. 2007) and HI cosmic density (Rhee et al. 2016, 2018) at a given redshift and using DEVILS-derived environmental metrics to explore the effect of environment on atomic gas content and distribution (e.g. Cortese et al. 2011; Brown et al. 2017; Poggianti et al. 2017).

4 TARGET SELECTION

In the following section, we provide a detailed description of the imaging, source extraction and photometry, colour-based selection of potential stars and galaxies, masking, and visual inspection. We refer the casual reader to Section 5 for a brief summary of how our final sample was selected.

4.1 Imaging

We use VISTA *Y*-band imaging for our input selection band from UltraVISTA (D10) and VIDEO (D02 and D03). The UltraVISTA data used in our sample were taken between 2009 and 2012 with VIRCAM Y, J, H, Ks, and NB118 bands covering the central 1.5 deg^2 of the COSMOS region (D10). The survey uses a 'jitter' image technique to produce 0.15″/pix plate-scale image resolution. The observing strategy of UltraVISTA produced deep and ultra-deep (0.62 deg^2) stripes covering the COSMOS region to 24.8, 24.5, 24.1, and 23.8 mag in the deep stripes and 25.7, 25.4, 25.1, and 24.9 mag for the ultra-deep stripes in Y, J, H, and Ks, respectively (5σ 2″ apertures). We note that even the deep stripes consist of data 3.5 magnitudes fainter than our survey limit. Full details of the UltraVISTA survey and data characteristics can be found in McCracken et al. (2012).

VIDEO data are taken with VIRCAM Z, Y, J, H, and Ks bands covering a total of 12 deg^2 covering ECDFS (D03), Elais-S1, and XMM-LSS (D02). Data are stacked and re-sampled to obtain a 0.2″/pix image resolution. We use the most recent (February 2017) VIDEO internal team data release that provides stacked images in all five bands and SExtractor-derived (Bertin & Arnouts 1996) colour-optimized photometry catalogues. The 2017 data reach 5σ 2″ aperture detection limits of 25.43, 24.96, 24.54, 24.05, 23.67 (D02) and 24.76, 24.92, 24.52, 23.88, 23.57 (D03) in Z, Y, J, H, Ks, respectively. Full details of the VIDEO survey and data characteristics can be found in Jarvis et al. (2013). Fig. 7 displays the DEVILS regions (red box) in relation to the UltraVISTA and VIDEO imaging.

4.2 ProFound source finding and extraction

To form a complete $Y < 21.2$ mag sample, we must derive robust total photometric measurements for all sources in the DEVILS regions. In addition, to perform our photometric star–galaxy separations, we also require Y, J, H, and Ks colour-optimized photometry.

Traditionally, widely used source detection software, such as SExtractor, would be used to identify target sources and extract photometry. However, within the GAMA survey (see Wright et al. 2016) and our G10/COSMOS analysis (see Andrews et al. 2017), we have found that SExtractor produces a non-negligible number of erroneous detections/measurements that require significant manual intervention (see previous references for in-depth examples). To overcome some of these issues, we have developed a new source detection and extraction code ProFound (Robotham et al. 2018). Briefly, ProFound identifies peak flux positions within the image, performs watershed deblending to identify source 'segments', and then iteratively grows (dilates) these segments to measure total photometry. For full details of the ProFound package and comparison to other source detection algorithms, see Robotham et al. (2018).

For our input photometry, we ran a bespoke wrapper to the base ProFound code that splits target images into a number of subregions, identifies sources, extracts photometry, and then recombines the outputs to produce photometric measurements for the full survey region. This avoids some memory issues with deep imaging containing a large number of sources and allows the code to be run in an easily parallelizable fashion.

To perform source extraction with detailed deblending of flux, we would ideally like to identify all potential sources of flux in a given region, extending well below the proposed survey limit. While our sample requires only the identification and extraction of targets to $Y < 21.2$ mag, much fainter sources may lie close to these on sky and thus require identification and extraction to remove their

[4]https://project.lsst.org/sites/default/files/WP/Gawiser-ultradeep-extragalactic-01.pdf

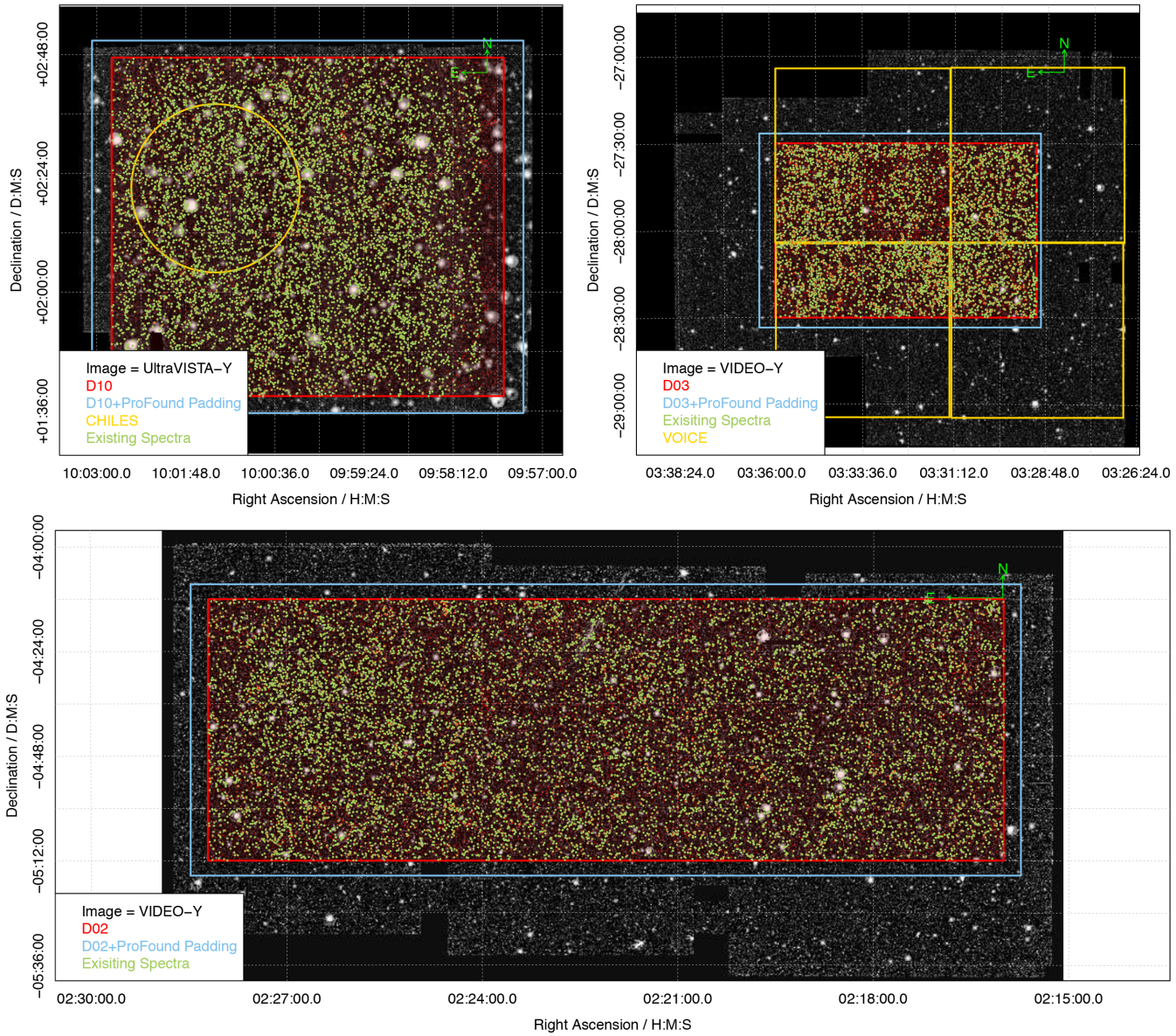

Figure 7. DEVILS fields in relation to NIR VISTA *Y*-band imaging from VIDEO (D02, D03) and UltraVISTA (D10). Existing robust spectroscopic redshifts at $Y < 21.2$ mag are shown as faint green dots. The red box bounds the DEVILS field, while the blue box highlights the region over which we perform our PROFOUND source finding (as not to exclude sources that overlap the DEVILS field boundary). Gold regions display new, ongoing surveys that have driven our choice of region selection – the CHILES HI survey in D10 and VOICE VST imaging survey in D03.

(potentially contaminating) flux. To maximize the removal of these confusing sources and to provide a more robust identification of the segments required for a total flux measurement (extending to the low-surface brightness wings of sources), we produce an inverse variance weighted stacked image using the VISTA Y, J, H, and Ks images. We first run PROFOUND independently over each band to determine a band-specific sky-RMS map. We then weight each image by its sky-RMS^{-2} and combine to form a deep combined YJHKs image. This image does not conserve flux but is used only to identify source segments to faint surface brightness limits (not to measure photometry).

Using the stacked image, we run PROFOUND with default parameters except: tolerance = 0.8 and skycut = 1.5 to produce a segmentation map containing all segments to very faint magnitude limits (∼25 mag in the *Y* band). These PROFOUND parameters were found to improve the segmentation in the deeper and 'jittered'/resampled VISTA imaging of UltraVISTA and VIDEO, where the PROFOUND defaults were tuned to the shallower and 0.34″/pix resolution VISTA Kilo-degree Infrared Galaxy, VIKING. The tolerance parameter allows for less source fragmentation at higher resolutions, and the skycut parameter allows segments to extend to the lower surface brightness wings of sources in the deeper data (see Robotham et al. 2018, for further details of these parameters). PROFOUND is run over the DEVILS regions with an ∼0.5 deg padding to measure photometry for any sources that fall at the edge of the DEVILS region (bounded by the blue box in Fig. 7).

To derive our total NIR multiband photometry, we then take the segmentation map defined using our stacked image and measure the total flux in each segment in the Y, J, H, and Ks bands separately. However, there are a number of potential pitfalls to consider

measuring multiband photometry, such as matching the photometric aperture across bands, and accounting for point spread function (PSF) and seeing differences across the image/bands (see discussions in Driver et al. 2016b; Wright et al. 2016). For our sample, these effects are minimal. The VISTA data are pixel-matched in each field, and thus to first order, we can simply apply the stacked segments to the pixel data in each band individually. However, this does not account for small differences in PSF and seeing. To account for this, we recalculate the sky value in each band independently and allow the segments to dilate to include extended flux if necessary with up to six dilations (iters = 6) but not shrink (see Robotham et al. 2018, for a detailed description of this process). Allowing this dilation can account for slightly varying PSFs for different bands and across the image but does not significantly alter the segment used.

In all bands, we record the default PROFOUND output parameters, including the total flux, average surface brightness to a radius containing 90 per cent (R90 – where the radius is defined as the elliptical semimajor axis) and 50 per cent (R50) of the source flux, magnitude, segment statistics (such as axial ratio, R50, R90, number of pixels in segment, etc), and segment flags (such as the number of pixels that border another segment or the edge of the frame). Fig. 8 displays the PROFOUND segments identified in a subregion of the UltraVISTA data for the *Y*-band image to full depth (left) and to our $Y < 21.2$ mag limit (right). We also overplot SEXTRACTOR apertures from the publicly available UltraVISTA catalogues. Even at the relatively bright DEVILS limit, SEXTRACTOR produces erroneous apertures in crowded regions, leading to incorrect total photometry; PROFOUND does not suffer from these issues. However, note that in the main UltraVISTA papers they do not directly use these apertures for their scientific analysis but opt for fixed-size colour-optimized apertures (see comparisons below).

4.2.1 *Colour-optimized photometry*

In addition to the total photometry outlined above, we also measure colour-optimized photometry in all bands using PROFOUND. For this colour-optimized photometry, we ideally wish to measure flux in a fixed size aperture covering the central, high-surface brightness region of the source, where colour gradients are minimal (i.e. we only require that our measurement is consistent across all bands but does not require a total flux). When PROFOUND identifies sources, it produces an initial (undilated) segmentation before dilating to obtain a total flux measurement. By design, these 'undilated' segments cover the central high-surface brightness region of each source and are therefore ideal for colour-optimized photometry (see Robotham et al. 2018). We take the fixed size undilated segments derived from our stacked YJHK image and apply to each band individually. We once again recalculate the sky background independently for each band but do not allow any dilations (iters = 0) to preserve the size/shape of each segment. Comparisons of our colour-optimized photometry with the VIDEO/UltraVISTA fixed-aperture photometry are presented in Section 4.4.

4.3 Photometric Re-calibration

In order to ensure accurate magnitude zero-point scaling, both in terms of selection in our input band and for NIR colour-based star–galaxy separation, we perform our own independent zero-point verification and scaling. We undertake this in a two-step process, using observed Two Micron All Sky Survey (2MASS Cohen, Wheaton & Megeath 2003) magnitudes to calibrate the J, H, and Ks bands independently in each field and then using the COSMOS2015 (Laigle et al. 2016) Y-J colours to calibrate the *Y* band.

2MASS provides a stable NIR flux calibration and is used in the VISTA data reduction performed by the Cambridge Astronomy Survey Unit (CASU). In each field, we take all 2MASS sources and perform a 2″ positional match to our PROFOUND catalogue in J, H, and Ks. To directly compare default 2MASS (Vega) and VISTA-VIRCAM (AB) measurements, we apply the magnitude system/colour scalings detailed on the CASU VISTA photometric calibration web page.[5] Both VIDEO and UltraVISTA surveys are processed using CASUVERS 1.3 and as observed with the same facility/instrument require the same colour terms:

$$J_{\rm VISTA} = J_{\rm 2MASS} + 0.937_{\rm VEGA-AB} - 0.077(J-H)_{\rm 2MASS}$$

$$H_{\rm VISTA} = H_{\rm 2MASS} + 1.384_{\rm VEGA-AB} + 0.032(J-H)_{\rm 2MASS}$$

$$Ks_{\rm VISTA} = Ks_{\rm 2MASS} + 1.839_{\rm VEGA-AB} + 0.01(J-Ks)_{\rm 2MASS}$$

where VEGA-AB terms are the conversion between Vega and AB magnitudes. We then calculate the median magnitude offset of PROFOUND – 2MASS at $14.75 < {\rm Mag}_{\rm ProFound} < 16.5$ (given in Table 2), applying the offsets to each band/field independently. Fig. 9 shows the resultant recalibrated comparison between PROFOUND and 2MASS. We see good agreement between 2MASS and PROFOUND in all bands and all zero-point corrections applied in J, H, and Ks are <0.06 mag. We also note that there is very little evidence for zero-point non-linearity in the data, which would manifest as a non-linear offset in our calibration region (the distribution of blue points at $14.75 < {\rm Mag}_{\rm ProFound} < 16.5$ has little or no gradient).

As 2MASS does not observe in the *Y* band, we cannot directly compare to 2MASS to calibrate our *Y*-band zero-point. However, within the COSMOS2015 analysis of Laigle et al. (2016), they derive robust NIR colours for all sources in COSMOS by calculating zero-point offsets in comparison to a library of galaxy templates. As such, any systematic offset in Y–J colour between the COSMOS2015 catalogue and our recalibrated PROFOUND Y–J colours is likely due to a zero-point offset in Y. We select COSMOS2015 galaxies at $Y < 21.2$ mag and perform a 2″ match to our PROFOUND catalogue. Using the matched sources, we calculate the median Y–J colour in both COSMOS2015 and our catalogue. We then take the systematic offset between median values as our *Y*-band zero-point scaling given in Table 2. Note that, the VIDEO team has performed its own independent analysis and determined an ~ 0.1 mag offset in its *Y*-band zero-point (provided via private correspondence from VIDEO P.I. M. Jarvis and noted in the VIDEO ESO data release document) – this is consistent with the offset we obtain here.

4.4 Comparisons to existing photometry

Our primary aim in this process is to obtain consistency in colours and *Y*-band normalization across all fields, both for our initial input *Y*-mag selection and for our photometric star–galaxy separation. In Fig. 10, we show a direct comparison between our PROFOUND photometric measurements and those for the COSMOS2015 catalogues in D10 and our own independent SEXTRACTOR run on the VIDEO data using default SEXTRACTOR setting for D02 and D03. We do not use the VIDEO team's internal catalogues as they use SEXTRACTOR parameters optimized for colour, not total, photometry ($>3\sigma$ for both

[5] http://casu.ast.cam.ac.uk/surveys-projects/vista/technical/photometric-properties

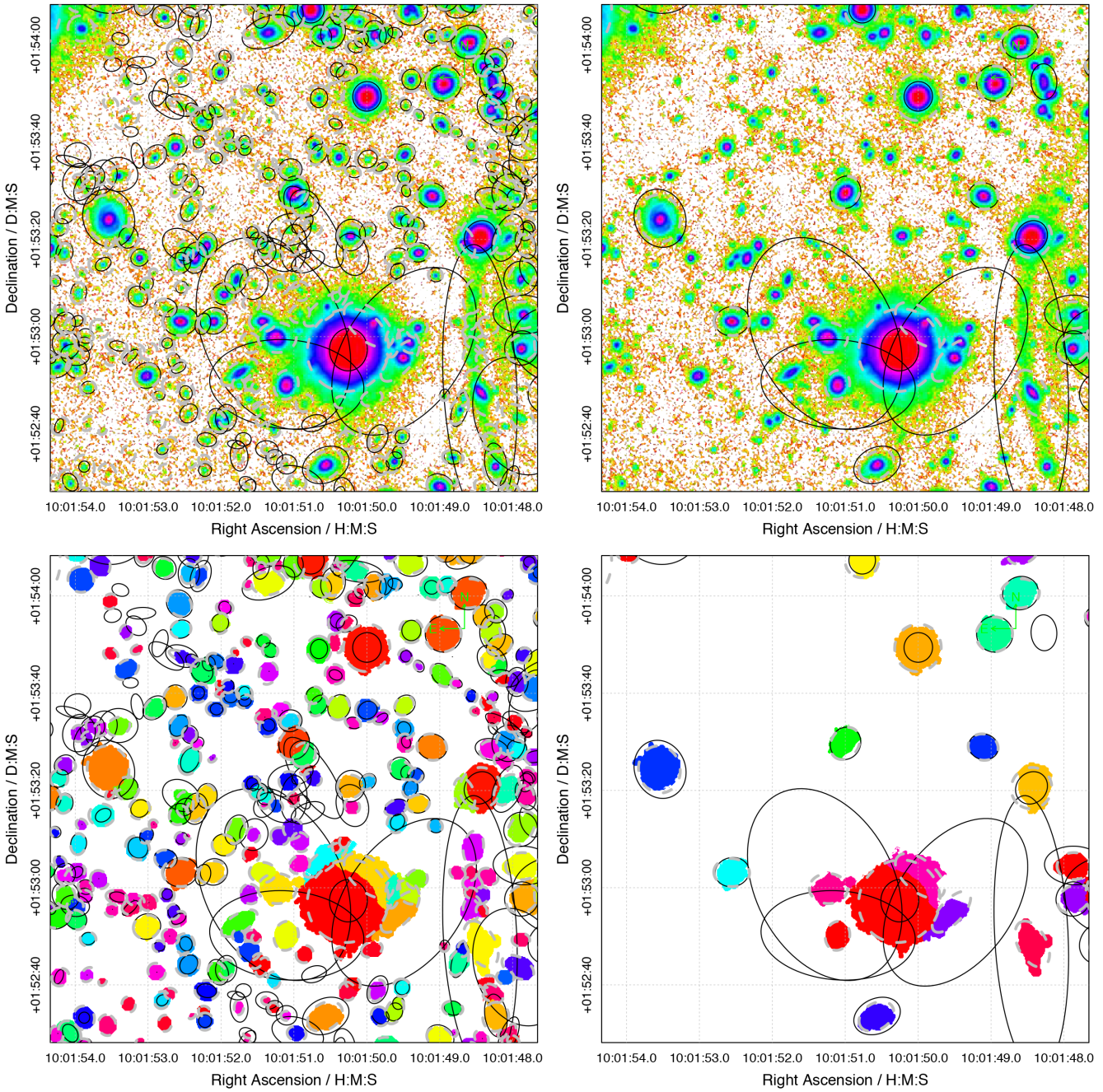

Figure 8. PROFOUND source detection and extraction in a complex subregion of D10. Top left: Input UltraVISTA image with rainbow colours used to display pixel flux, overplotted as black ellipses are SEXTRACTOR-defined apertures from the UltraVISTA catalogues. Bottom left: PROFOUND segments identified in the same region (coloured by unique ID). We also overplot in grey an ellipse defined by the PROFOUND segment; although this is not used in our analysis. The SEXTRACTOR-defined catalogue contains false detections (i.e. around 10:01:53.5, 01:53:55 – top left), erroneously large apertures where multiple sources are identified as single source (i.e. around the complex region at 10:01:50.4, 01:52:50), misses flux in the extended wings of some sources (i.e. the source at 10:01:50, 01:53:45), and identifies the large stellar halo (bottom right) as a bright source. The right two panels display the same as the left but for a DEVILS-like $Y < 21.2$ mag selection. Clearly, many of these same issues persist even at relatively bright magnitudes.

detection and analysis thresholds leading to significant missed flux but robust colours). We also display sources that are colour selected (see Section 4.5) as stars and galaxies in blue and red, respectively.

All data points have the zero-point scaling outlined in the previous section applied, and we display all sources to $Y < 22$ mag (0.8 mag fainter than our DEVILS magnitude limit). For the D10 comparison (top four panels), we find excellent agreement in photometry between the COSMOS2015 catalogues and our PROFOUND photometry. All bands show no normalization offset across the full magnitude range and tight interquartile range to faint magnitudes ($\lesssim$0.2 mag). The COSMOS2015 team also uses a stacked (zYJHKs) image for its source detection and aperture definition. For the D02 and D03 comparison to our SEXTRACTOR runs, we find offsets of $\sim$0.02–0.1 mag (increasing to fainter magnitudes), with PROFOUND typically measuring more flux than SEXTRACTOR. This is likely to be caused by two effects: (i) a systematic effect of SEXTRACTOR

Table 2. Zero-point scaling applied to NIR data in DEVILS Fields. All offsets are additive.

Field	Imaging Survey	Band	Zero-point offset	Method
D02	VIDEO	Y	0.0943	COSMOS2015 Y-J colour
D02	VIDEO	J	0.0512	2MASS J magnitude
D02	VIDEO	H	0.0442	2MASS H magnitude
D02	VIDEO	Ks	0.0498	2MASS K magnitude
D03	VIDEO	Y	0.1000	COSMOS2015 Y-J colour
D03	VIDEO	J	0.0510	2MASS J magnitude
D03	VIDEO	H	0.0537	2MASS H magnitude
D03	VIDEO	Ks	0.0421	2MASS Ks magnitude
D10	UltraVISTA	Y	0.0474	COSMOS2015 Y-J colour
D10	UltraVISTA	J	0.0489	2MASS J magnitude
D10	UltraVISTA	H	0.0230	2MASS H magnitude
D10	UltraVISTA	Ks	0.0270	2MASS Ks magnitude

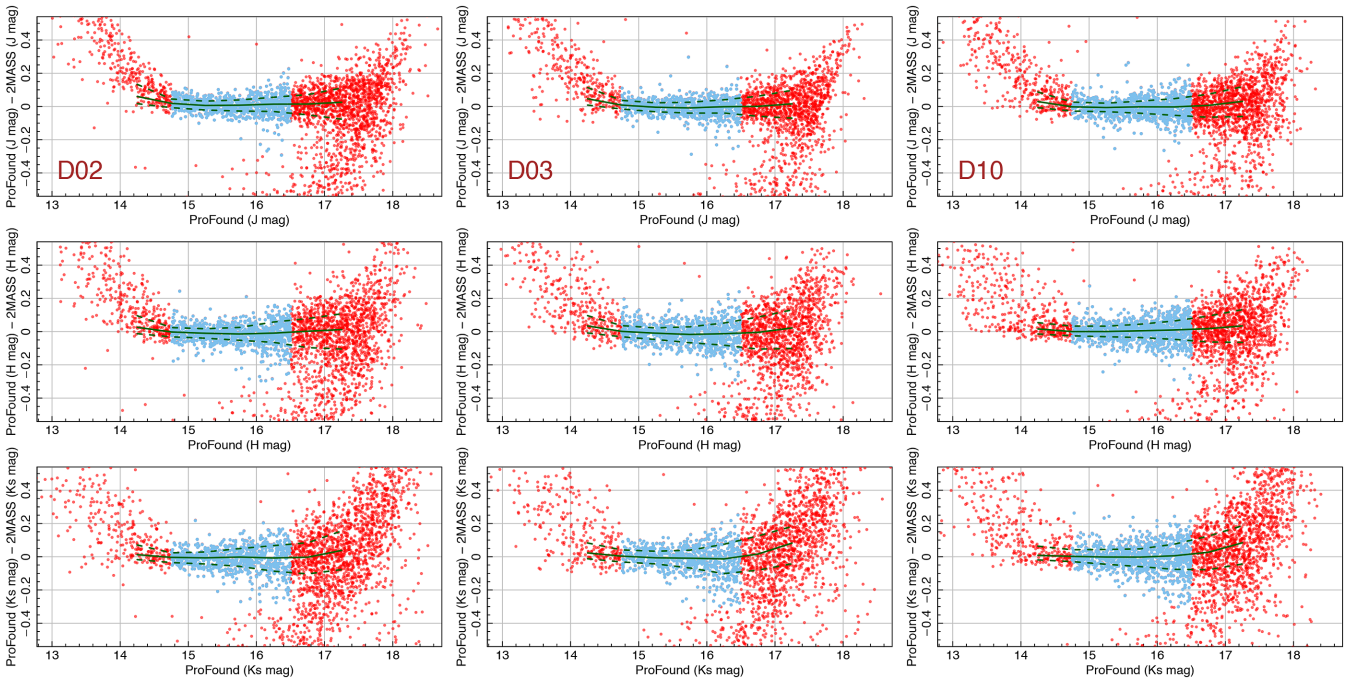

Figure 9. ProFound magnitudes compared to 2MASS magnitudes in J, H, and Ks after zero-point scalings given in Table 2 have been applied. Data used for zero-point scaling are highlighted in blue. Running median and interquartile range are displayed as solid and dashed line, respectively. The median interquartile range for the blue calibration points is ∼0.08, 0.1, and 0.1 in J, H, and Ks, respectively. The upwards tail at the bright end is due to bright stars being saturated in VISTA, while the scatter/upwards tail at the faint end is due to low-SN in the 2MASS data and aperture/segment and seeing difference between VISTA+PROFOUND and 2MASS. We ignore both these regions in our zero-point calibration.

using Kron (Kron 1980) magnitudes, which typically can miss 1–10 per cent of the total flux – equating to magnitude offsets up to 0.1 mag, and (ii) the combination of using a stacked detection image and PROFOUND's methodology including the additional flux in the low-surface brightness (LSB) wings of sources. This additional flux could potentially influence the faint galaxy number counts and in turn their contribution to the extragalactic background light (EBL, see Driver et al. 2016a). This will be explored further in Section 4.8.

In order to perform our photometric star–galaxy separation, we also require reliable galaxy colours. Both the COSMOS2015 and VIDEO team catalogues produce fixed aperture photometry specifically designed to provide robust colours. In Fig. 11, we display the NIR colour distributions for our PROFOUND total photometry measurements (top six panels) and our colour-optimized photometry measurements (bottom six panels) only for sources colour-selected as galaxies. For total photometry, we compare to the COSMOS2015 and VIDEO points used in Fig. 10, while for colour photometry, we compare to each team's fixed 2″ aperture measurements. For each distribution, we calculate the median, standard deviation, normalized median absolute deviation (NMAD or 1.4825 × MAD), and outlier rate. Outliers are defined as sources with absolute colour at >2× the standard deviation away from the median.

First, taking the total photometry measurements, we find that PROFOUND produces consistent median colours to both COSMOS2015 and our VIDEO-SEXTRACTOR runs to within 0.004 mag (D10 – COSMOS2015) and 0.02 mag (D02 and D03 – VIDEO). We also find that our standard deviation, NMAD, and outlier rates are comparable or slightly lower than both COSMOS2015 and VIDEO-SEXTRACTOR.

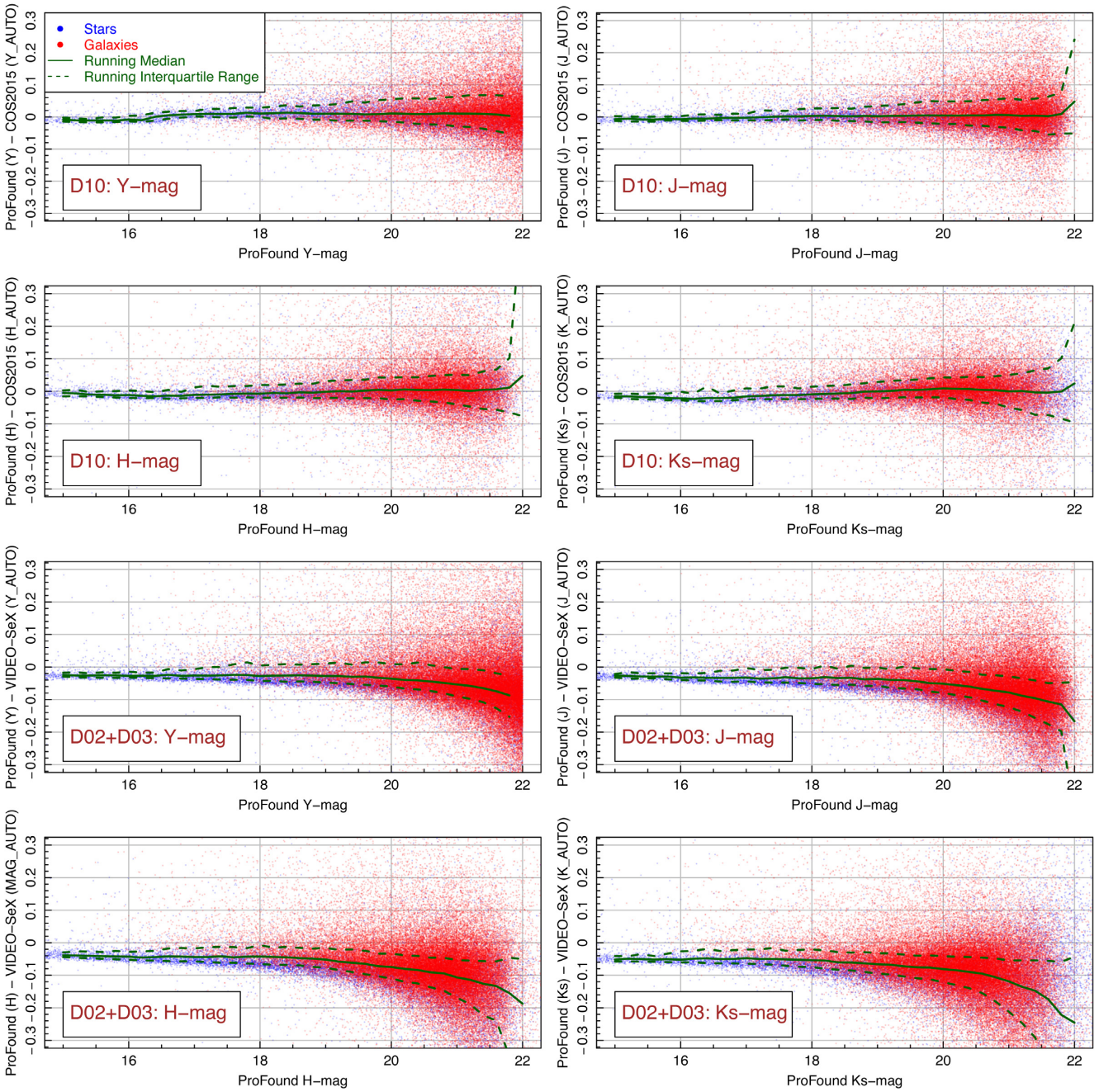

Figure 10. ProFound magnitudes compared to VIDEO (SExtractor default runs) and UltraVISTA (COSMOS2015 catalogues) magnitudes in Y, J, H, and Ks after zero-point scalings given in Table 2 have been applied to both data sets. Sources are split into stars (blue) and galaxies (red) using the colour-based star–galaxy separator outlined in Section 4.5. Note that the magnitudes measured in both VIDEO and COSMOS2015 are not optimized for total magnitudes and thus the small normalization offsets are expected. Our ProFound runs are extremely consistent with the COSMOS2015 measurements across the full magnitude range. In D02 and D03, ProFound consistently measures more flux than SExtractor, with this offset increasing to fainter magnitudes. This is likely due to the fact that ProFound is measuring further into the low-surface brightness wings of sources.

For the colour-optimized photometry, we find slightly larger offsets in median colour of 0.02 mag (D10 – COSMOS2015) and 0.07 mag (D02 and D03 – VIDEO). However, in most cases, our standard deviation and NMAD values are consistently smaller than both COSMOS2015 and VIDEO, highlighting that ProFound is producing accurate colour photometry for our star–galaxy separation. We also find that our ProFound colours are consistent across the UltraVISTA (D10) and VIDEO (D02 and D03) imaging to <0.08 mag with the largest offset in Y–J colour.

4.5 Star–galaxy separation using NIR colours

The outputs of ProFound provide us with a wealth of information with which to perform colour-based star–galaxy separation (NIR colours, surface brightness, axial ratio, etc. See Robotham et al. 2018). We note that sources selected in this manner are not spectroscopically confirmed stars and galaxies, and as such our selections identify only potential stars and galaxies. However, for clarity, from here on we shall refer to our colour-selected samples as stars and galaxies.

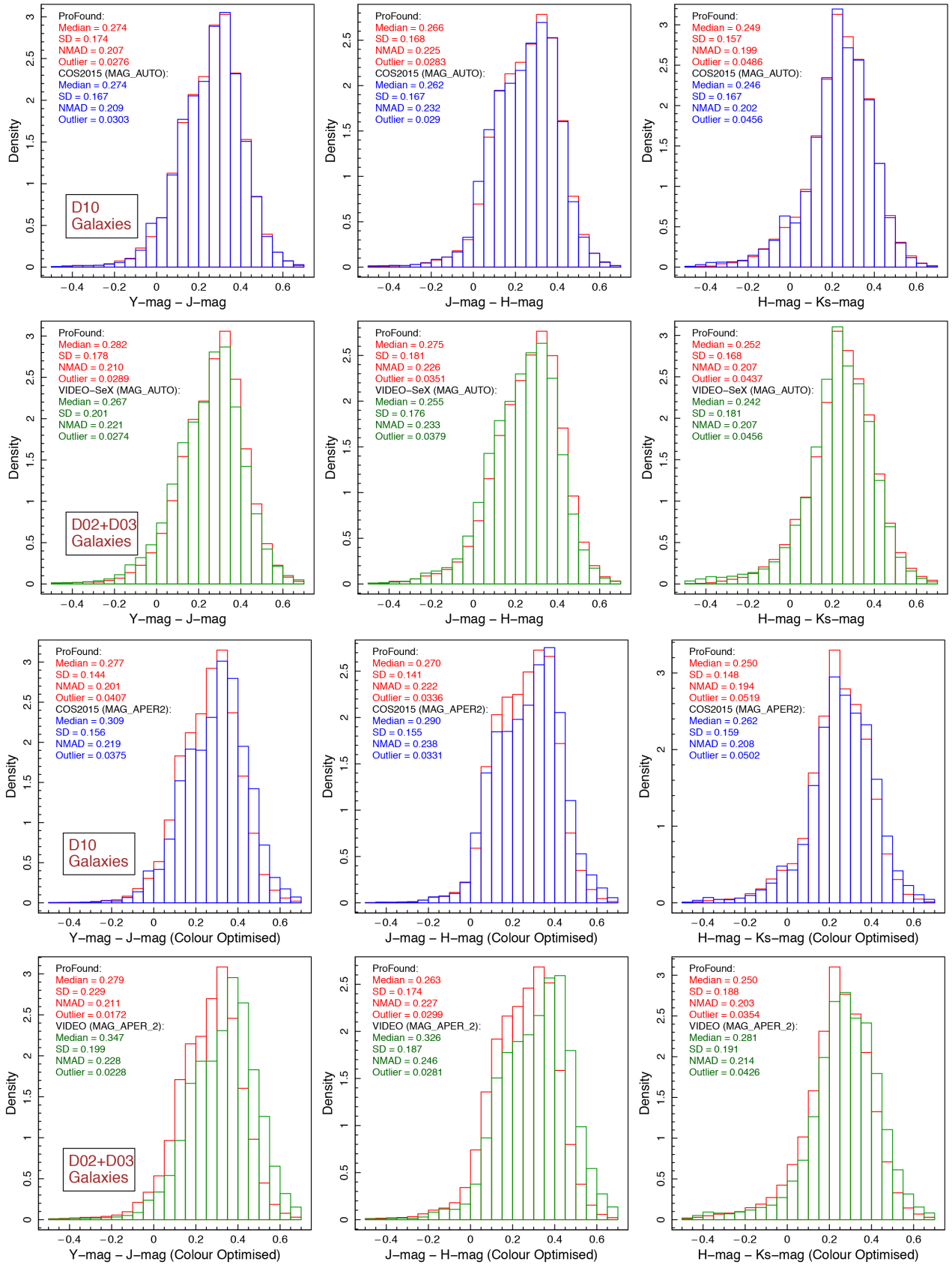

Figure 11. Colour comparison between PROFOUND and VIDEO/COSMOS2015 after zero-point scaling for total photometry measurements (top two rows) and colour-optimized photometry measurements (bottom two rows). For total photometry, we compare PROFOUND to the MAG_AUTO parameters in the COSMOS2015 catalogue and our VIDEO SEXTRACTOR default runs on the D10 and D02/D03 data, respectively. For colour-optimized photometry, we use the undilated segments from PROFOUND and fixed 2″ aperture measurements from both the COSMOS 2015 catalogue and VIDEO team's internal catalogue.

Following a number of tests using various parameters, we determined that the cleanest star–galaxy separation is produced when using a combination of NIR colours, with a bright surface brightness cut for saturated stars and a faint surface brightness cut to include galaxies with large photometric errors at the low-surface brightness end. Note that these faint sources do not meet the DEVILS $Y < 21.2$ mag selection limit and thus are not in our final sample. Figs 12 and 13 display our star–galaxy separation procedure for all PROFOUND sources and just those that meet the DEVILS $Y < 21.2$ mag selection limit, respectively. The former of these is used only for our number counts (see below).

To define our colour star–galaxy separation, we take our colour-based PROFOUND photometry (see Section 4.2.1), derive the distribution of (H–Ks)–(Y–J) colours for all sources that meet our magnitude selection (left column of Fig. 13), and determine the trough point between the two peaks. The blue and red peaks identify stars and galaxies, respectively. We note here that this binary cut at the trough point will exclude a small number of galaxies. However, following this we do perform further visual classifications of all sources in the trough region to identify these sources (see Section 4.6). The distribution of these galaxies/stars in comparison to axial ratio and average *Y*-band surface brightness to the radius containing 90 per cent of the source flux, $Y\mu_{90}$, are shown in the middle and right columns of Fig. 13. We do find that there are a small number of saturated stars that meet our NIR colour selection criteria, so we apply an additional, $Y\mu_{90} > 18$ mag arcsec^{-2} cut for galaxies. In Fig. 12, we also find that when pushing well below the DEVILS limit, galaxies with large error on their photometric measurements encroach on the stellar track. As such, we apply an additional $Y\mu_{90} < 24.5$ mag arcsec^{-2} cut to our stellar selection when determining our number counts. In summary, to select galaxies we use:

$$(H - Ks) - (Y - J) > -0.26 \text{ OR } Y\mu_{90} > 24.5 \text{ mag arcsec}^{-2}$$

$$Y\mu_{90} > 18 \text{ mag arcsec}^{-2}.$$

The validity of colour star–galaxy selection will be discussed further in Section 4.6 where we perform visual classifications on all sources in the D10 region using high-resolution *HST* data.

One potential caveat to using a colour-based star–galaxy separation is that strong emission lines from star formation/AGN can potentially cause galaxies to have stellar-like colours at specific redshifts and thus be removed from our sample (see Atek et al. 2011, for the effect of strong emission line sources on NIR colours). While we perform additional visual classifications in Section 4.6, which aim to quantify these misidentifications, it is interesting to consider the types of sources and redshifts that may be affected. H α at 6568 Å is the most prominent line emission that may significantly affect the colours used in our star–galaxy separation. At $0.5 < z < 0.7$, H α falls within the *Y* band and with sufficient line luminosity could alter our NIR colours. However, in using a (H–Ks)–(Y–J) colour selection, an increased *Y*-band flux would only redden the colour and such an object would still be selected as a galaxy. However, at $z \gtrsim 0.85$, H α transitions to the *J* band and would act to make that galaxy colours closer to that of stars. At $z \gtrsim 0.96$, the [OIII] 5007 Å line, which is also associated with strong star formation, also transitions to the *Y* band and, for comparable EWs, the effect of emission lines of Y–J colour is negated. Hence, only strongly star-forming and AGN sources at $0.85 < z < 0.96$ may potentially have their colours significantly affected and be identified as stars in our star–galaxy separation. If resolved, these sources will be identified in our visual classifications. However, for unresolved sources with star-like colours, separation between stars and galaxies is problematic. We note that such galaxies would appear as roughly uniformly blue-scattered points about the galaxy locus in Fig. 13 (as they are likely to have a range of line luminosity). However, there does not appear to be a large number of sources scattered below our star–galaxy separator line. This is unsurprising as the on-sky number density of sources like those discussed in Atek et al. (2011) are extremely low and as such, we predict that the misclassification of such sources is unlikely to significantly affect our sample.

4.6 Visual classification

4.6.1 Initial HST *visual classification in D10*

To test the validity of our colour-based star–galaxy separation and to remove any additional artefacts from our input catalogue, we perform a visual classification. While we would ideally like to undertake visual classifications using high-resolution imaging (such as *HST*), such data are not available over all of the DEVILS area. However, we can use the deep *HST* imaging in D10 (COSMOS) to identify regions of parameter space which require further visual classification and to compare visual classification to those obtained via the VISTA imaging alone. For example, are sources that are colour selected as galaxies but appear small, compact, and spherical in the VISTA imaging truly galaxies or stars when viewed with *HST*? To this end, we visually classify *ALL* ∼30 000, $Y < 21.2$ mag sources (both stars and galaxies, prior to masking) in the D10 region using both a NIR three-colour image (Y, J, Ks) and single-band *HST* F814W image. We generate postage stamps of all sources and visually classify them as a star, galaxy, or artefact/confused photometry/subregion of galaxy in both images separately (see Fig. 14).

We find that our initial colour selections are extremely robust at identifying stars and galaxies down to Y∼21.2 mag, as only 1.4 per cent of colour-selected stars appear to be galaxies in the *HST* imaging, and only 1.6 per cent of colour-selected galaxies appear to be stars. We also find that the majority (> 95 per cent) of sources classified as artefact/confused photometry/subregion of galaxy are in our masked regions, with the rest being subregions of a larger structure. However, a caveat is that this applies only for the magnitude range covered by the DEVILS sample ($Y < 21.2$ mag).

Using these *HST*-based classifications, we can therefore define regions within our NIR colour space with which to perform further visual classifications in our other fields (where *HST* data are not available for the full region) and potential pitfalls in identifying galaxies as stars and vice versa when only VISTA imaging is available. Fig. 15 displays the NIR-colour versus axial ratio used in our initial star–galaxy separation. Based on our colour selection and visual classifications, we colour-code sources that were not correctly defined using colour alone (i.e. galaxies that have stellar colours and/or stars that have galaxy colours). Unsurprisingly, the majority of these misclassifications sit very close to the star–galaxy separator dividing line. We define two regions of this parameter space where we can robustly isolate stars and galaxies (shaded regions in Fig. 15). There are a small number of red stars that cover the galaxies part of this parameter space (blue triangles that fall in the upper grey-shaded region). However, these will not bias our sample as they will simply be additional stars that we spectroscopically observe (and then remove). This will very marginally increase our total observation time. Given these sources cannot be identified a priori without *HST*-resolution data, and we do not have these

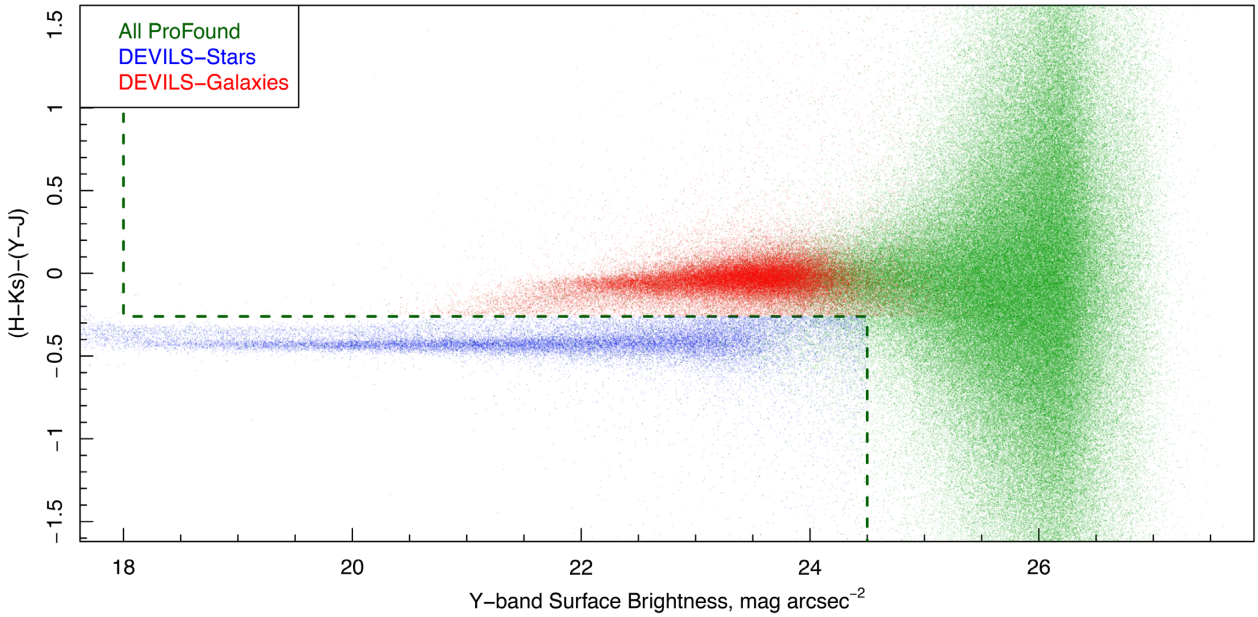

Figure 12. Star–galaxy separation using NIR colours and surface brightness for all PROFOUND-detected sources in D02, D03, and D10 combined. All PROFOUND detections are shown in green, while galaxies/stars that meet our $Y < 21.2$ mag selection are shown in red and blue, respectively. Our stellar selection window, as described in Section 4.5, is bounded by the green dashed box.

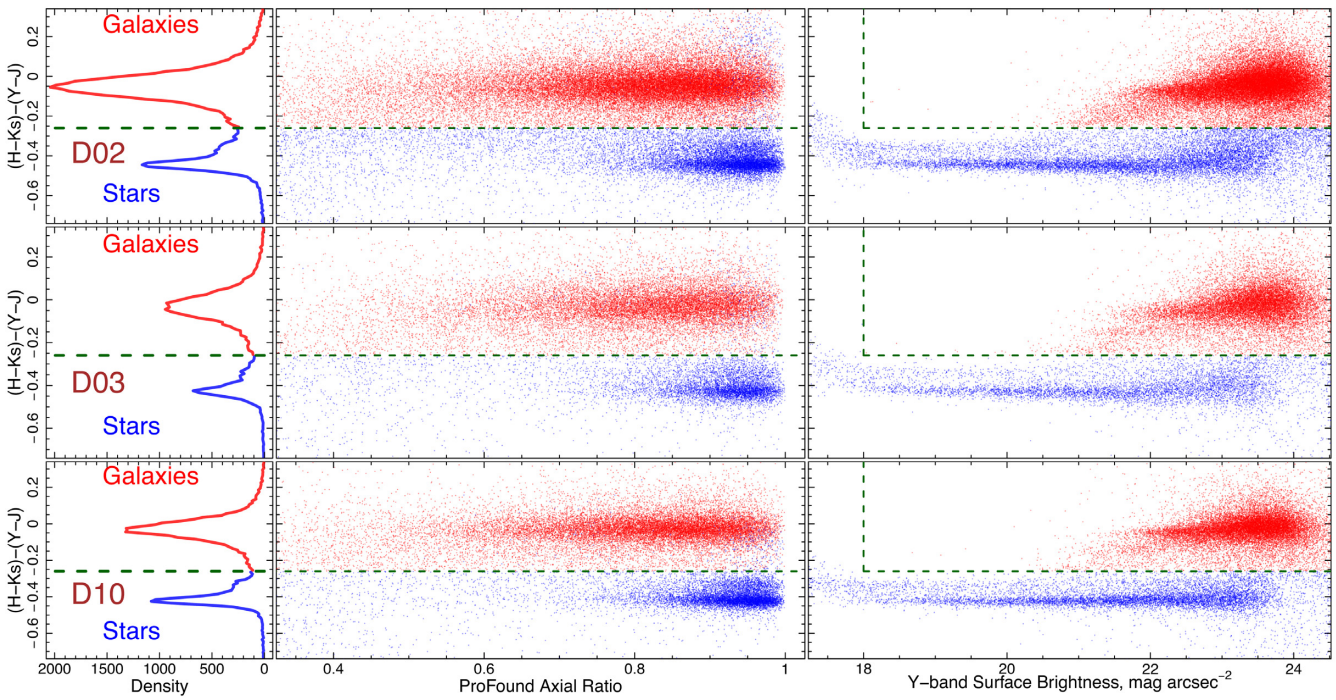

Figure 13. Star–galaxy separation using NIR colours and surface brightness for DEVILS $Y < 21.2$ mag sources in D02, D03, and D10 (top to bottom, respectively). Left: Histogram of (H–Ks)–(Y–J) colours in each field. We define the trough point between the two peaks as our colour separator between stars and galaxies. Middle: NIR colour against axial ratio (Y band) with galaxies and stars in red/blue, respectively. Right: NIR colour against surface brightness (Y band). Red and blue points are identical to Fig. 12. In addition to our NIR colour separation, we also apply a surface brightness >18 mag arcsec^{-2} selection for galaxies to exclude saturated stars. Note that sources with stellar colours and large axial ratio are largely identified as artefacts in out visual classifications.

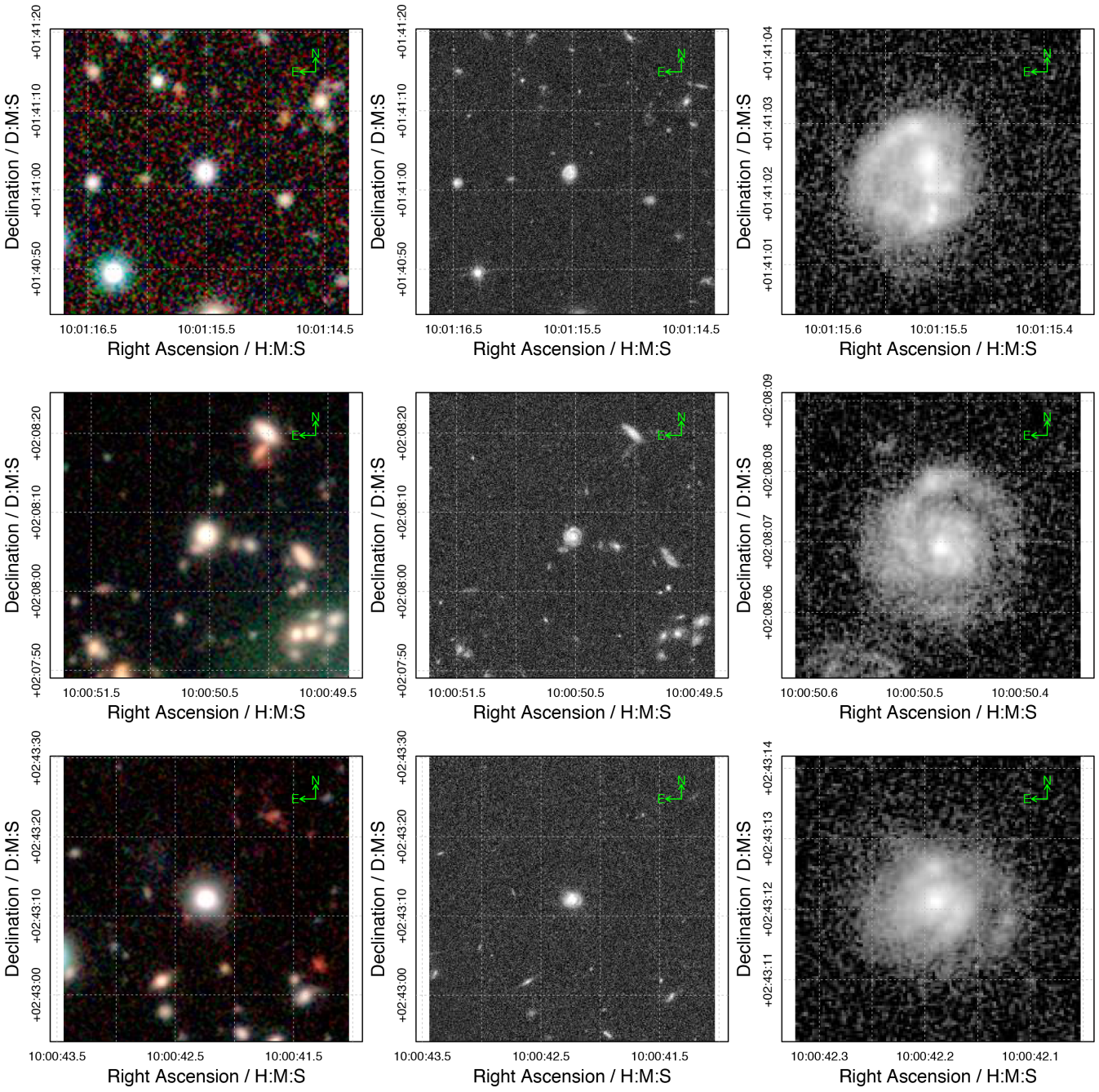

Figure 14. Examples of how galaxies could potentially be visually misidentified as stars when using NIR data alone for visual classifications. Left: UltraVISTA Y, J, Ks rgb images centred on an unresolved, spherical source in the UltraVISTA data. Middle: *HST* F814W image of the same region. Right: Zoom in of *HST* image at the position of the galaxy. In terms of visual classification, the central sources are largely indistinguishable from stars in the VISTA images alone (the blue source in the bottom left hand corner of the top row is a star). However, *HST* resolution imaging reveals that the central sources are all galaxies with clearly defined spiral structure. All rows are plotted over the same size regions.

data over all of the DEVILS area, they remain within our target sample.

For our final visual classifications, we inspect all sources outside of these two regions in all three DEVILS fields. Note that for our final input catalogues we repeat the visual classifications in D10 without the aid of *HST* data to be consistent across all regions. Thus, we visually inspect all sources that *do not* meet one of the following criteria.

Robust galaxies:

$$-0.17 < (H-Ks)-(Y-J) < 0.2 \;\&\; AxialRatio > 0.475.$$

Robust stars:

$$-0.6 < (H-Ks)-(Y-J) < -0.3 \;\&\; AxialRatio > 0.725.$$

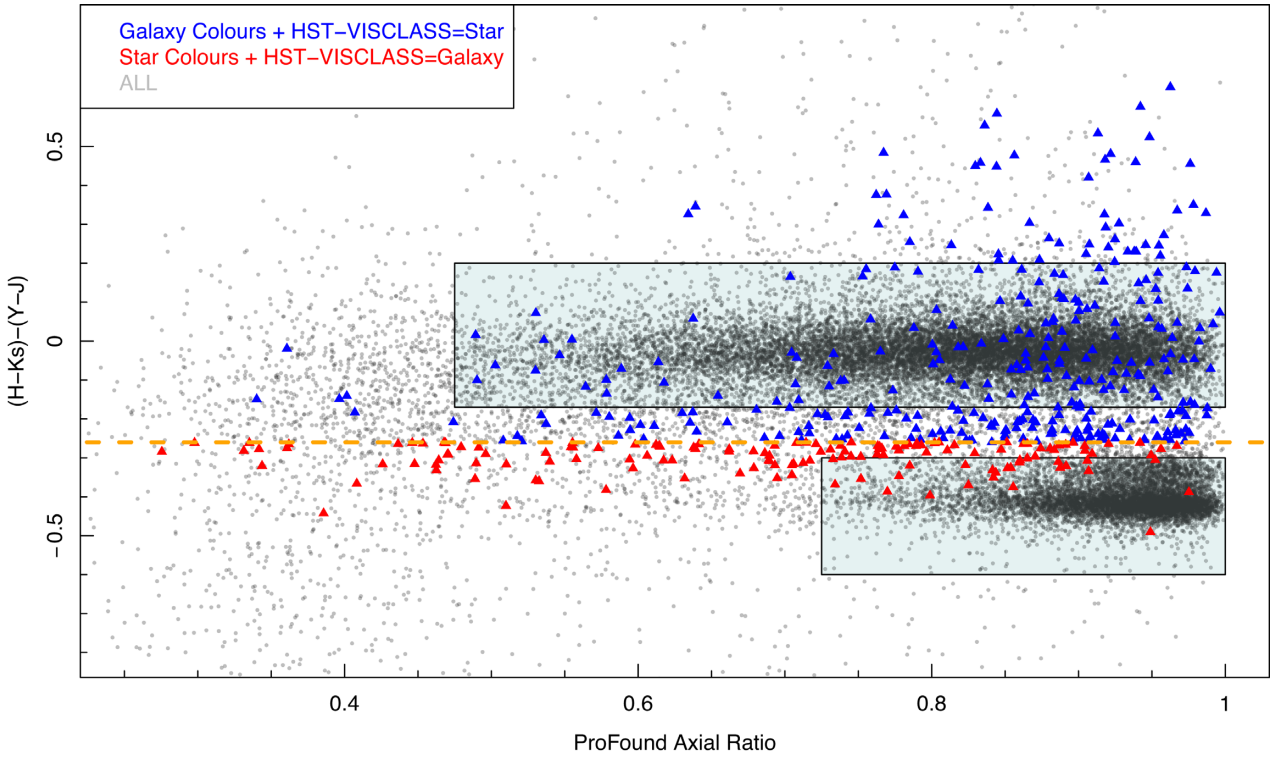

Figure 15. Visual classifications using *HST* imaging in D10. Grey points display all $Y < 21.2$ mag sources in D10, with our initial star–galaxy separator displayed as the dashed orange line. Blue points display sources that were NIR colour selected as galaxies but appear to be stars when visually inspected using *HST* resolution data. Red points display sources that were NIR colour selected as stars but appear to be galaxies when visually inspected using *HST*. Note that red and blue points are displayed with larger symbols and no transparency to highlight their location. The grey-coloured sample dominates in number over all coloured points in almost all regions of this figure. Unsurprisingly, the majority of misclassified stars and galaxies sit close to the star–galaxy separation line. The two shaded boxes represent regions of this parameter space where we can robustly separate stars and galaxies using NIR colour and axial ratio.

As noted above, D02 and D03 have only the VISTA imaging to perform our visual classifications (no contiguous *HST* data exist over the full region). As such, we explore some potential pitfalls in VISTA-based classifications using a comparison between *HST* and VISTA in D10. The most striking example of this is that almost all sources that are red in our three-colour images but appear spherical and unresolved turn out to be galaxies when inspected in *HST*. Fig. 14 shows examples of such cases. Thus, when visually inspecting the NIR three-colour images in all fields, we take care to not misclassify galaxies as stars based on their unresolved nature. For the DEVILS input catalogue, we wish for our sample to be highly complete and will not be significantly affected by a low level of stellar contamination. Thus, our visual classifications will be aimed at only removing robustly identified stars, artefacts, and subregions instead of removing potentially ambiguous sources. In cases where a classification is unclear, we opt to retain the source in our sample.

4.6.2 Final NIR visual classifications in all fields

Following the process outlined in the previous section, we select all sources that fall outside the two regions described in Fig. 15 and are not in the masked regions described in Section 4.7 (leaving ∼9000 sources for visual classification) and produce postage stamp NIR three-colour images. We then visually classify these sources as stars, galaxies, or artefacts/subregions of galaxies, and assign these flags to our master input catalogue. We find that of 8945 sources visually inspected, 1065 change their initial NIR colour classification between star–galaxy (592 star to galaxy, and 473 galaxy to star). To be conservative in the process, we do not remove the small number of sources that are visually classified as stars from our sample but include only additional sources that are visually classified as galaxies.

4.7 Masking

Within the VISTA imaging used to select targets in our sample, instrumental effects in the optics produce ghosting and haloes around bright stars (as in all Cassegrain-style telescopes). These regions cause increased sky brightness, poor source detection, and confused photometry (see Fig. 16). As such, we mask the regions around bright stars in our input catalogue. In producing this mask, it is important to quantify the area of each field that is masked in order to perform any analyses using volume/area (i.e. Section 4.8).

The PROFOUND outputs provide useful parameters with which to identify bright halo regions. Here we use the segment SKYMEAN value in our *Y*-band PROFOUND run, which gives the local sky background at each segment position. In regions of bright haloes, this sky value is elevated above the background level (see top right panel of Fig. 17). We find that to optimally mask regions in the VISTA data, we require different mask parameters for UltraVISTA and VIDEO due to the different depths of the data. For UltraVISTA, we identify all segments where SKYMEAN $>1.8\times$SD[SKYMEAN] and mask a 250-pixel ($85''$) radius region around the centre of the segment. In regions with large bright haloes, multiple masked 250-pixel regions overlap to form a large masked region. This process also masks non-circular regions of scatter light, such as reflections. While this process captures

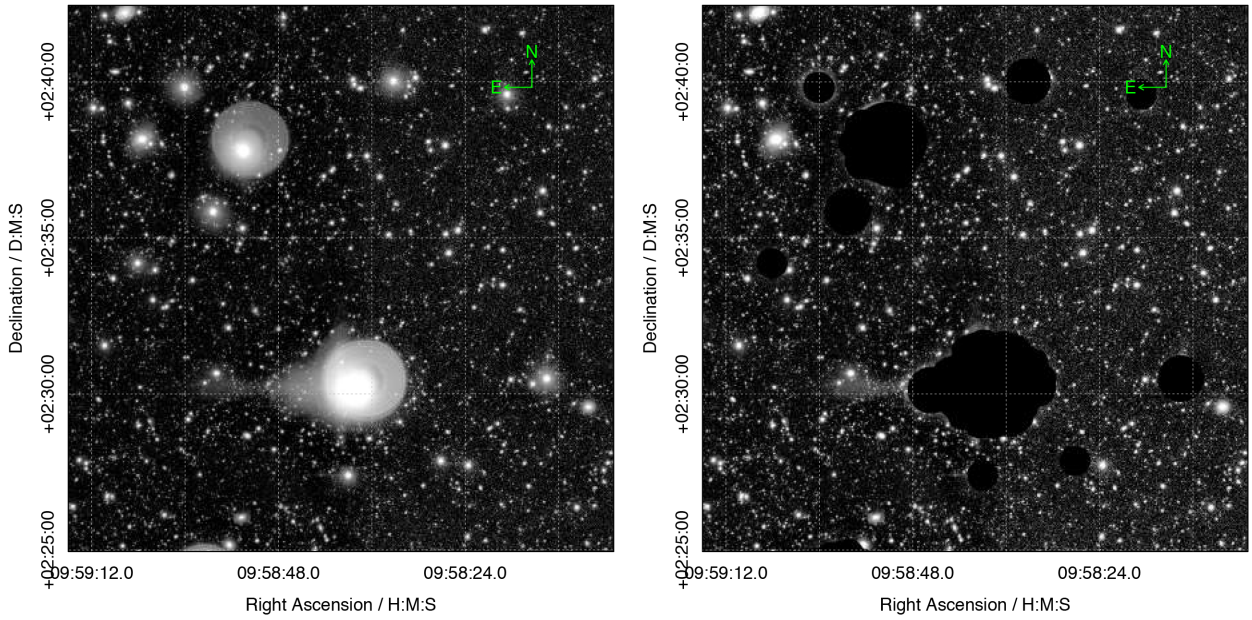

Figure 16. Left: Example of bright haloes around stars in UltraVISTA *Y*-band image. These haloes can cause increased sky brightness, poor source detection, and confused photometry, and thus must be masked. Right: The same region after masking.

large bright haloes, it does miss some smaller haloes around stars. In a second step, we also identify all stars with *Y*-band surface brightness, $Y\mu_{90} < 20$ mag arcsec^{-2}, and $Y < 13.25$ mag. These sources are also masked with a 200-pixel (68″) radius region. For VIDEO, we repeat this process using a SKYMEAN >2.25 ×SD[SKYMEAN] cut and 150/100 pixel regions, respectively. In an additional step, we find that the UltraVISTA data have some very large bright haloes that are offset radially from the bright star that produces them and are not fully encompassed by the above process. We identify these regions visually and apply an additional 500-pixel (170″) radius mask to the halo. Note that all mask sizes and selections have been optimized by trial and improvement to remove artefacts in the data.

Finally, we mask out regions of the DEVILS fields that are close to the edge of a VIRCAM pointing (i.e. the bottom left corner of the D10 field shown in the top left panel of Fig. 17) and regions of the VISTA imaging that sit outside of the DEVILS target region. Fig. 17 displays the masking process in the D10 field. The top right panel shows the distribution of high SKYMEAN values across the field, the bottom left panel shows the binary mask generated by our bright halo/source identification, and the bottom right panel displays the field with mask applied. In Table 3, we detail the resultant masked areas. For how this affects the number of target sources, see Table 4.

4.8 Faint NIR number counts

As an additional, albeit coarse, verification of our PROFOUND photometry, zero-point scaling, and star–galaxy separation, we also calculate the faint NIR number counts for our Y, J, H, and Ks photometry. Note that this does not include our visual classifications as this process is performed only on the DEVILS $Y < 21.2$ mag sample, and here we wish to investigate the number counts to much fainter magnitudes.

We take all sources identified in our PROFOUND catalogues and apply our star–galaxy separation discussed in the previous section, see Fig. 12. We bin in $\delta m = 0.5$ mag and use a total DEVILS area of 6.045 deg^2. In order to estimate errors, we assume that our sources are predominately from $0.2 < z < 1.0$ and calculating a cosmic variance error of 5.4 per cent using equation 4 from Driver & Robotham (2010), we linearly combine this with the Poisson error in each bin (as in Driver et al. 2016a). Fig. 18 displays the PROFOUND-derived number counts in all four VISTA bands. For comparison we overplot the compendium of data from Driver et al. (2016a) collated from GAMA, G10/COSMOS, and various *HST* programs (see Driver et al. 2016a, for details). For the Driver et al. points, we include their random, fitting, zero-point, and cosmic variance errors. The DEVILS number counts are consistent with the Driver et al. results in the 17 <mag<22 regime, which covers the bulk of our spectroscopic target sample. Most notably, we see an excess in the faint number counts at mag>22, suggesting an additional contribution from faint galaxies that could significantly contribute to the EBL (i.e. see Driver et al. 2016a). This is potentially due to the increased flux being detected by PROFOUND over SEXTRACTOR for faint galaxies, as described in Section 4.4, the potential lack of normalization consistency between the diverse array of data compiled by Driver et al. (2016a) – i.e. we find an excess in the number counts at the point where the Driver et al. (2016a) relations transition between GAMA/G10-COSMOS measurements and those derived from *HST* and/or inadequate separation of stars and galaxies at these faint magnitudes (see below). We do also see a small decrement in all of the number counts at the very bright end (mag<17), which is potentially due to the fragmentation of bright sources in the PROFOUND runs (which will be amended in our visual classifications) or the choice of these deep fields avoiding bright nearby structures. However, our final sample contains only a very small number of sources in this magnitude range as previous spectroscopic surveys have already targeted this population in the DEVILS regions.

As a crude validation of our star–galaxy separation, we also overplot the number counts for stars in the DEVILS regions in

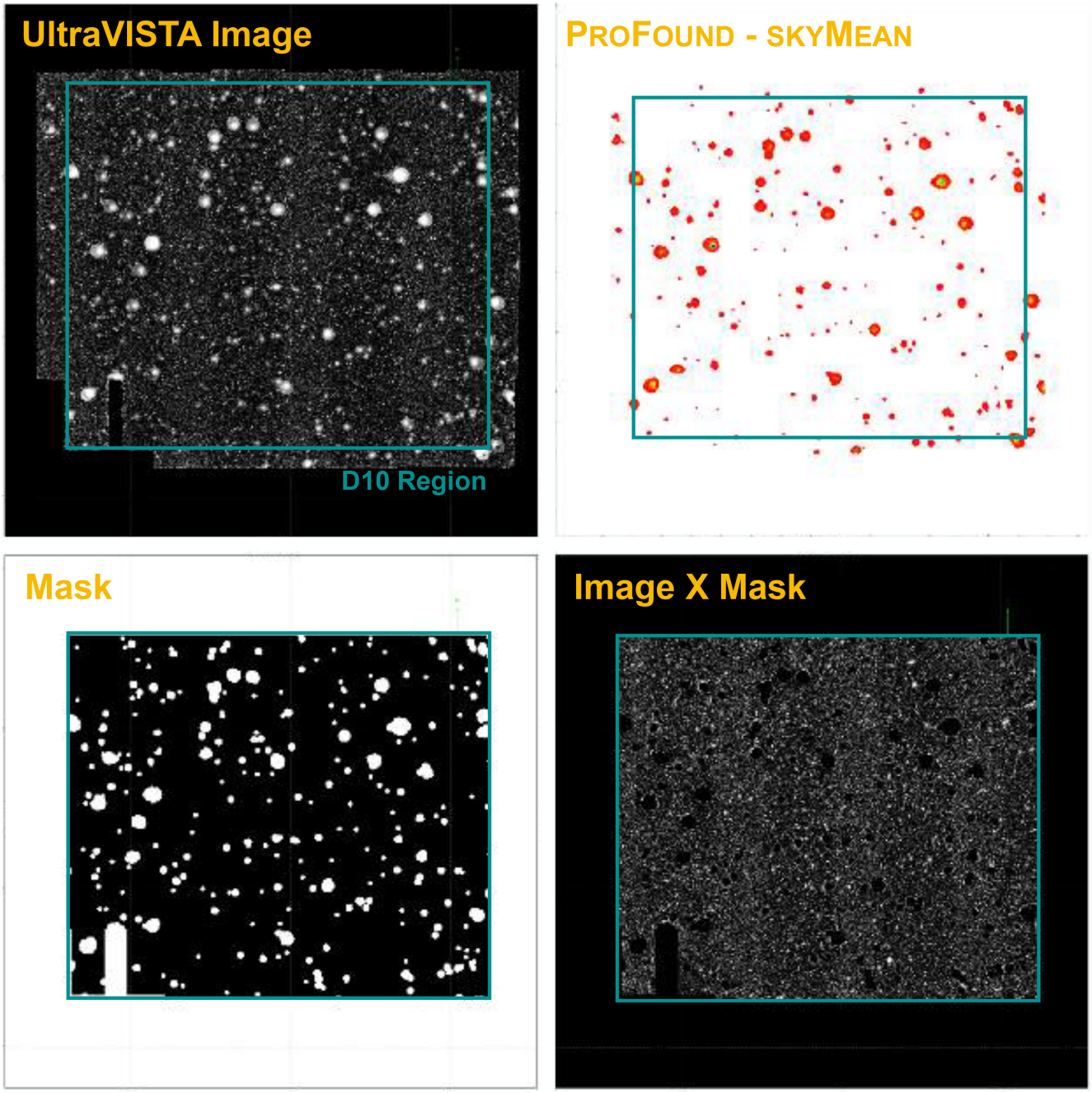

Figure 17. Masking process in D10. Top left: UltraVISTA *Y*-band imaging in COSMOS, green box displays the D10 field. Top right: The distribution of high PROFOUND – SKYMEAN values across the field. Bottom left: The binary mask generated by our bright halo/source identification (white = masked regions). Bottom right: The field with mask applied.

Table 3. Area of fields masks in bright star/halo masking.

Field	Total (deg)	Masked (deg)	Unmasked (deg)	Fraction Masked
D02	3.040	0.214	2.825	0.076
D03	1.501	0.086	1.415	0.061
D10	1.504	0.136	1.368	0.099

comparison with the models from the TRIdimensional modeL of thE GALaxy (TRILEGAL,[6] e.g. Girardi et al. 2005). To simulate our DEVILS stellar number counts with TRILEGAL, we supply the position and size of each of the DEVILS regions and combine to take into account the varying stellar density as a function of field position. In all bands, the model stellar number densities are comparable to our star counts, most notably in the *Y* band where we perform

[6]http://stev.oapd.inaf.it/cgi-bin/trilegal

Table 4. Summary of generation of target catalogues. Col2: Total number of segments identified by PROFOUND in the region. Col 3: Total number of PROFOUND with $Y < 21.2$ mag. Col 4: Number of segments identified as potential galaxies and stars using the colour selection outlined in Section 4.5. Col 5: Number of colour-selected stars and galaxies in masked region. Col 6: Number of colour-selected stars and galaxies in unmasked region. Col 7: Number of sources visually classified as stars, galaxies, and artefacts (total inspected = 8945 – artefacts include erroneous sources, subregions of bright galaxies that have been split by PROFOUND, in these cases, we ensure that the centre of the galaxy is still included in our sample and sources that are very close to a bright source and are likely to have their photometry compromised). Col 8: Existing number of sources with redshifts, total number if the total at $Y < 21.2$ mag in the region and sample is the number in our final sample. Col 9: Final DEVILS target sample for AAT observations (colour-selected galaxies in unmasked regions that currently do not have a redshift, plus sources with stellar colours but visually appear to be galaxies).

Field	ProFound Segments	$Y < 21.2$ Segments	Colour Sel (Gals/Stars)	Masked (Gals/Stars)	Unmasked (Gals/Stars)	Vis-Class (Gals/ Stars/Artefacts)	Previous (total/sample)	Final Targets
Section 3.3 (col 1)	Section 4.2 (col 2)	Section 4.2 (col 3)	Section 4.5 (col 4)	Section 4.7 (col 5)	Section 4.7 (col 6)	Section 4.6 (col 7)	Section 5.1 (col 8)	Section 5 (col 9)
D02	1 197 887	51 078	36 048/14 662	4413/3106	31 635/11 556	2812/1128/1440	9630/7838	21 602
D03	568 333	24 585	17 052/7350	2209/1601	14 843/5749	1230/456/637	4713/3830	10 040
D10	811 366	29 597	19 607/9926	2799/1933	14 657/902	857/93/294	6867/6419	7575
Total	**2 577 589**	**105 260**	**72 707/31 938**	**9421/6640**	**61 135/18 207**	**4899/1677/2369**	**21 210/18 087**	**39 217**

our target selection and at $17.5 < Y < 21.2$ mag, where the majority of our targets lie. We do note that our stellar number counts are somewhat steeper than those found in the deep *HST* data from the Great Observatories Origins Deep Survey South field (Windhorst et al. 2011). They obtain a slope of ∼0.045 dex/mag at NIR wavelengths for 17<NIR-bands<25 mag, in comparison to our ∼0.1 dex/mag at for 17<NIR-bands<21.5 mag. However, considering fig. 11 of Windhorst et al. (2011), we find that at NIR wavelengths, the flattening of the stellar number counts occurs prominently at >20 mag and there are large error bars at <19 mag. Overplotting our number counts on those from fig. 11 of Windhorst et al. (2011), we find them to be completely consistent within errors in the 17.5 <NIR bands<21.2 mag regime.

We note that the cutoff in our stellar counts at mag>22 is largely due to our $Y\mu_{90} < 24.5$ mag arcsec^{-2} cut in star–galaxy separation. At fainter surface brightnesses, it becomes difficult to distinguish between stars and galaxies in the VISTA data alone. However, we note that if we simply use our total source number counts (star + galaxies) and subtract the TRILEGAL model in each magnitude bin, it does not fully account for the discrepancy in the faint galaxy number counts in comparison to Driver et al. (2016a) noted previously. We do not go into a detailed analysis of the separation of stars and galaxies and their number counts at these faint magnitudes that are well below the DEVILS limit (>22 mag), as a detailed description of the faint number counts from DEVILS and their implication will be presented in Koushan et al. (in preparation).

5 FINAL INPUT CATALOGUES

5.1 Spectroscopic target list

Following all of the analysis in Section 4, we produce a final input catalogue of targets for AAT spectroscopy using the following identification and selection criteria:

(i) Source was identified and segment parameters defined by PROFOUND using a stacked Y, J, H, and Ks VISTA image (Section 4.2).

(ii) Source *total* photometry measured by PROFOUND after zero-point scaling and galactic extinction correction with Y<21.2 mag (Section 4.2 and 4.3).

(iii) Source *colour* photometry measured by PROFOUND has (H–Ks)–(Y–J)>−0.26 and $Y\mu_{90} < 24.5$ mag arcsec^{-2} (Section 4.5).

(iv) Source *Y*-band surface brightness measured by PROFOUND has $Y\mu_{90} > 18$ mag arcsec^{-2} (Section 4.5).

(v) Source does not fall in a masked region of the image (Section 4.7).

(vi) If visually inspected, the source is classified as a galaxy (Section 4.6).

This leaves an initial sample of 57 304 DEVILS targets. Selected columns from the final DEVILS input catalogues (including all $Y < 21.2$ mag sources) are made public via the AAO data central archive[7] and are described in Table 5.

5.1.1 *Existing spectra*

Each of the three DEVILS fields was specifically targeted for the high number of previously spectroscopically targeted sources. We compile a robust list of these sources in each region and set the priority (P) of these objects to 1 (not to be observed). In this previous spectroscopic sample, we include in D02 and D03:

(i) Sources from the OzDES catalogue of confirmed redshifts. This includes a compilation of targeted OzDES observations, SDSS, GAMA, SNLS, DEEP2, 2dFGRS, PanSTARRS-AAOmega, VVDS, VIPERS, VUDS, and ongoing targeted observations in ECDFS carried out by the LADUMA team (Wu et al., in preparation) – for further details of these observations and catalogue, see (Childress et al. 2017).

(ii) In total, there are 9630 previous redshifts in D02 and 4713 previous redshifts in D03. Of these 7838 and 3830, respectively, are in our final target sample. These are assigned a priority of $P = 1$ (meaning not targetable).

and in D10:

(i) Sources from VVDS (Le Fèvre et al. 2014) ZFLAGS = 3 and ZFLAGS = 4.

(ii) Sources from zCOSMOS (Lilly et al. 2007) with Z_CC>2 and Z_CC<6, or Z_CC>12 and Z_CC<16, or Z_CC>22 and Z_CC<26. This includes spectroscopically confirmed primary targets, AGN, and secondary targets.

(iii) Sources from VUDS (Le Fèvre et al. 2013) quality flag>2.

(iv) Sources from hCOSMOS (Damjanov et al. 2018) with confirmed redshifts.

(v) In total, there are 6867 previous redshifts in D10. Of these, 6419 are in our final sample and are set to $P = 1$.

These spectroscopic observations and their composition will be described in detail in the first DEVILS data release paper.

[7] datacentral.aao.gov.au/services/query/

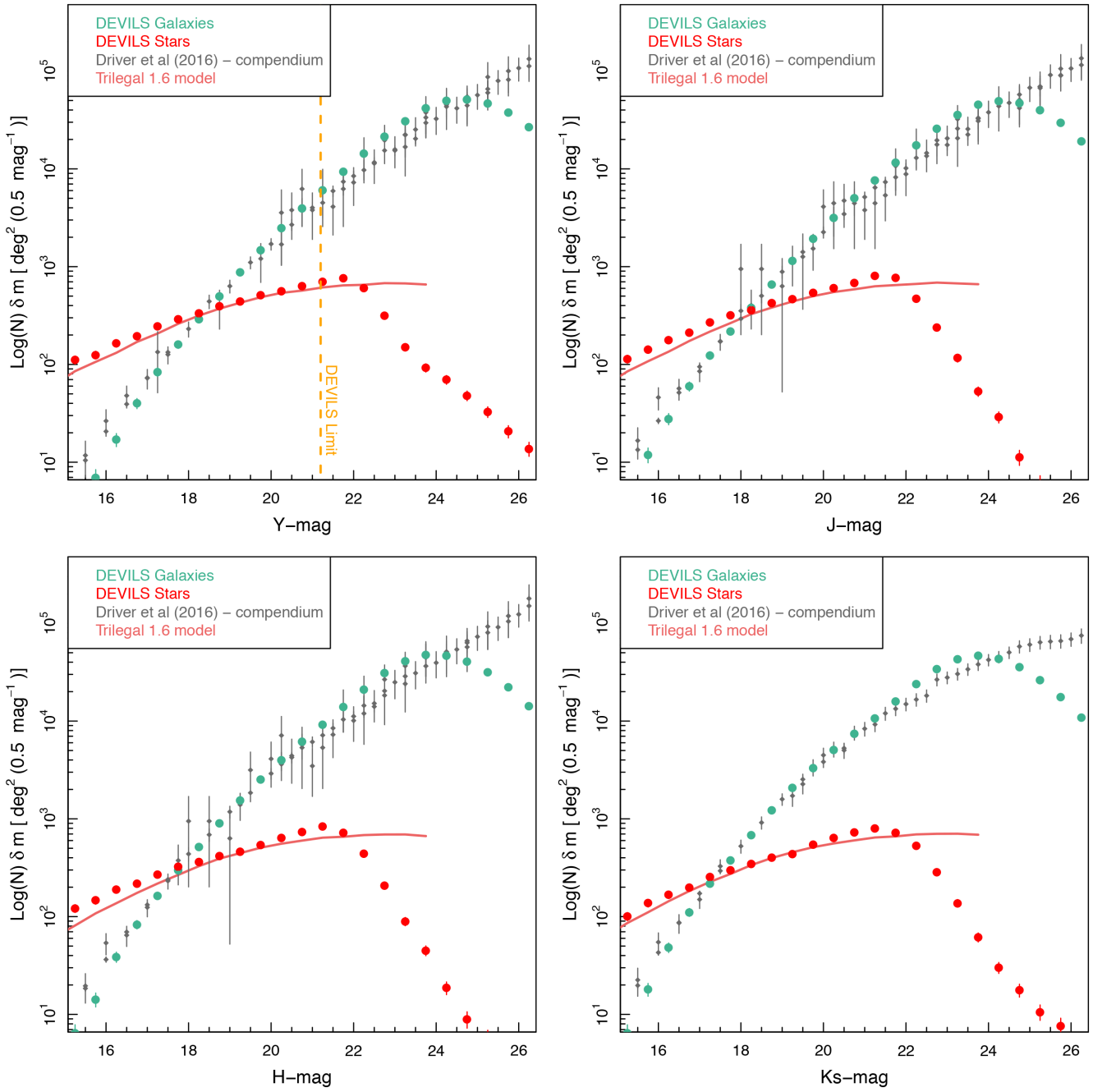

Figure 18. Faint NIR number counts derived from our PROFOUND source detection and extraction in the DEVILS regions for galaxies (green large points) and stars (red large points). We overplot the compendium of number counts from Driver et al. (2016a), grey small points, and find consistency over the majority of the magnitude range in our sample. We find an increase in the number density of faint sources (mag>22) in comparison to Driver et al. (2016a). We also overplot the TRILEGAL (see text) model stellar number counts as the red line.

5.2 Calibration sources

5.2.1 Sky fibres

In order to select sky fibre positions, we can also utilize PROFOUND. One of the PROFOUND outputs is an aggressively dilated object mask (OBJECTS_REDO), which masks all pixels that could potentially contain source flux. In order to space potential sky fibre positions uniformly within our fields, we consider each subregion processed through PROFOUND (see Section 4.2) independently. We select all unmasked pixels in the OBJECTS_REDO map that are classed as a sky pixel and do not border an object pixel. We then exclude all sky pixels that are within 20″ of a Y <21.5 mag object centre or within 1.5′ of a bright Y-mag<15 source. We then randomly select 10 potential sky fibre positions in each subregion and ensure that no two positions are within 1′ of each other. Lastly, we visually inspect all sky fibre positions to ensure that they do not contain source flux. This provides a total of 520, 241, and 420 potential sky fibre positions in D02, D03, and D10, respectively, which are passed to our fibre

Table 5. DEVILS input catalogue columns and description. Full catalogue is made publicly available at https://datacentral.aao.gov.au/services/query/.

Column name	Column descriptor	UCD	Units
CATAID	Unique DEVILS survey identifier	meta.id	None
FIELD	DEVILS Field	meta.code.member	None
VIDEOID	VIDEO ID of 2″ matched source	meta.id.cross	None
UVISTAID	UltraVISTA ID of 2″ matched source	meta.id.cross	None
COSMOS2013ID	COMSOS2013 ID of 2″ matched source in COSMOS2015 Catalogue	meta.id.cross	None
G10CATAID	G10COSMOS ID of 2″ matched source from (Andrews et al. 2017)	meta.id.cross	None
RA	Right Ascension of source in VISTA *Y* band	pos.eq.ra;em.IR.Y	Deg
DEC	Declination of source in VISTA *Y* band	pos.eq.dec;em.IR.Y	Deg
YMAG	VISTA *Y*-band magnitude	em.IR.Y	Mag
YMAGERR	VISTA *Y*-band magnitude error	stat.error;em.IR.Y	Mag
STARCLASS	Star-galaxy separation flag based on NIR colours and surface brightness (0 = Galaxy, 1 = Star)	meta.code.class	None
MASK_FLAG	Mask flag (0 = unmasked, >0 = masked)	meta.code.class	None
VISCLASS	Visual classification flag base on VISTA YJKs rgb images (0 = galaxy, 1 = star, 2 = artefact, 3 = shredded region of bright galaxy, 4 = near bright source with confused photometry, NA = not classified)	meta.code.class	None
AXRAT	Axial ratio of source defined from ProFound segments in VISTA *Y* band	phys.size.axisRatio;em.IR.Y	None
SB90	Average surface brightness to R90 in VISTA *Y* band	phot.flux.density.sb;em.IR.Y	Mag Arcsec^{-2}
NIRCOL	VISTA (H-Ks)-(Y-J) colour used in star-galaxy separation	phot.color	None

assignment algorithm. In each observation, we observe 25 blank sky positions.

5.2.2 *Flux standards*

We select flux standards in a similar manner to GAMA and OzDES. In both D02 and D03, we use identical flux calibration standards as OzDES, who select all F-class stars at 16.6 <r<18.4 mag (Yuan et al. 2015). Observing identical flux calibration stars to OzDES allows for a much more robust accuracy of the flux calibration. For D10, we use a similar selection to GAMA. Spectroscopic standards are selected from SDSS using (from the SDSS DR14 catalogue) fibermag_r > 16.9 and 16.6 < psfmag_r < 18.4 and classified as either SPECTROPHOTO_STD or REDDEN_STD. We observe three spectroscopic standards in each observation.

5.2.3 *Guide stars*

For guide stars, we select all sources at 13.7<R1Mag<14.4 sources from the USNO-B guide-star catalogue and exclude sources with proper motions of >15 mas yr^{-1}. We then perform a 2″ match to our PROFOUND catalogues and exclude all sources that would not be colour selected as stars. We then use the PROFFOUND RAcen and Deccen values as our guide positions to be consistent with our target astrometry (i.e. we use the VISTA positions of USNO-B-selected guide stars). All potential guide stars are visually inspected to ensure that they are isolated, single, unsaturated stars. In total, we obtain ∼100 potential guide stars per deg^2, of which 7–8 are selected in each pointing.

5.3 Tiling and fibre assignment

Targets are assigned priorities based on their *Y*-band magnitude, with fainter sources having higher priority: *Y*>21 mag = P7, 20 <*Y*<21 mag = P6, 19 <*Y*<20 mag = P5, *Y*<19 mag = P4. This allows objects that are likely to require more repeat observations to be preferentially targeted early in the survey. We then also produce a set of bad weather priorities that inverse these to preferentially target bright sources. Targets are assigned to fibres using the greedy tiling algorithm outlined in Robotham et al. (2010) and used extensively in GAMA (Driver et al. 2011; Baldry et al. 2012; Liske et al. 2015) and for the Sydney-AAO Multiobject Integral-field spectrograph (SAMI) Galaxy Survey (Bryant et al. 2015). This adds additional weights to priorities based on close on-sky clustering to allow complex regions with high levels of potential fibre collisions to be preferentially targeted. In the majority of cases, the 400 2dF fibres are allocated as follows: ∼360 targets, 25 sky, three standard stars, eight guides (remaining fibres broken or unusable).

6 SURVEY STRATEGY, DATA REDUCTION, AND 2017B OBSERVATIONS

6.1 Nightly observations

DEVILS targets were observed with the 2dF+AAOmega system on the AAT with program ID A/2017B/011. Fibre flat observations were taken with the Quartz_75_A, 75W lamp and arc observations with the FeAr_1, FeAr_2, CuAr_1, CuAr_2, CuHe_1, CuNe_1 lamps. Data are typically observed in a 6 s flat, 45 s arc, 2 × 1800 s sequence (modulo changes to weather and exact tile assignment at the start/end of the night). ∼30 dark frames are taken each run and 10 bias frames are observed each day.

6.2 Redshift feedback exposure times

Within the DEVILS survey, we do not use fixed total integration times based on prior information regarding each source. This is due to the fact that it is difficult to make a robust prediction for the exposure time required to obtain a redshift based on observed frame colour and magnitude alone (this will be explored in detail in further work). The required exposure time is a complex function

of spectral type (emission/absorption), line strength, and redshift (i.e. where key spectral feature falls within your observing window). If we wish to obtain a > 95 per cent completeness survey with no bias to spectral type using fixed exposure times, we would by necessity have to overexpose for many emission-line sources where these lines fall in easily observable, high-transmission regions of the spectral window. To overcome this, instead we adopt a new observing strategy that uses a short time-scale redshift-success feedback loop to maximize our survey efficiency. In this strategy, we observe each target on a 1-h time-scale and check for a secure redshift. If a redshift is confirmed, then the target is removed from our input catalogue; if not, the source is prioritized for a repeat observation on the following night. Multiple repeat observations are then combined prior to the redshift checks. In this manner, sources are observed only for the minimum (rounded up to the nearest hour) exposure time required to obtain a secure redshift (see Kafle et al. 2018, for our primary exploration of this method for the G15Deep sample).

Given CCDs with no read-noise, fast reconfiguration times, and availability of targets, this method would become maximally efficient with very short exposure times (i.e. with 15-min exposures one would never expose for >15 min longer than required to obtain a redshift). However, in practice each sub-exposure must be easily sky-noise dominated (as not to stack large contributions of read-noise in each sub-exposure), and long reconfiguration times and short exposures would lead to large overheads. For AAOmega at the AAT 1800 s sub-exposures are sufficiently sky-noise dominated and reconfiguration times of the 2dF fibre positioner are ∼45–50 min for our relatively complex configurations (reconfigurations are undertaken while observing as 2dF has two observing plates). The combination of these two time constraints necessitates minimum target exposure times of ∼1 h. Note that this process is also proposed for a number of the 4m Multi-Object Spectrograph Telescope (4MOST, de Jong et al. 2014) consortium surveys, the Taipan survey (da Cunha et al. 2017) and potential surveys undertaken with the Mauna Kea Spectroscopic Explorer telescope (MSE, McConnachie et al. 2016). Notably, 4MOST will suffer less from read-noise (newer CCDs) and reconfiguration time (4MOST's Australian European Southern Observatory Positioner, AESOP, has reconfigure times of <1min; Haynes et al. 2016) and thus will be able to explore shorter exposure time feedback loops.

6.3 Data reduction using the DEVILS tool for analysis and redshifting

The difficulty of observing in the mode discussed above is that we require our data to be reduced, redshifted, target catalogues updated, and new target configurations produced on a very short time-scale. The survey becomes maximally efficient if this process occurs on a ∼12 -h time-scale (i.e. redshift information from a night's observations is used to target for the following night).

In order to perform this short time-scale feedback, we developed the DEVILS Tool for Analysis and Redshifting (TAZ). Our pipeline allows data to be synced from the telescope to the DEVILS archive nightly, TAZ then reduces these data using the 2dFDR software package (see Croom, Saunders & Heald 2004; AAO software Team 2015) in a bespoke highly parallelizable fashion, spectra are extracted, repeat observations stacked, stacked spectra redshifted using AUTOZ (Baldry et al. 2014), target catalogues updated, and tiling files produced for the next night's observing.

Full details of our TAZ reduction will be presented in the first DEVILS data release paper. However, we simply note here that the pipeline takes ∼4−5 h to run from the raw data being added to the database to new fibre configuration files being uploaded to the telescope for the next night's observing with no human intervention. All raw and reduced data, extracted spectra, metadata, catalogues, logs, and diagnostic plots are written to the DEVILS database which exist in identical clones in both Perth and on the AAO Data Central system.

6.4 December 2017 and January 2018 observations

DEVILS observations began in December 2017 with 19 nights scheduled in the 2017B semester. While the detailed description of these observations will be outlined in our first data release paper, here we describe the primary results of the first observations and survey progress.

We typically observed six fibre configurations per night (three on half nights) targeting ∼2100 sources on a full night. As we prioritized faint (Y>21.0 mag) targets that require the longest exposure times, we observed 8856 unique sources over 80 different configurations and obtained 4353 secure redshifts. We lost ∼33 per cent of observing time to bad weather and a site evacuation due to forest fires. Our current observed-targets-to-redshift-success rate is only ∼50 per cent as we have prioritized the faintest sources in our sample, and many targets have not yet been observed to the integration time required to obtain a redshift. The currently confirmed redshifts and exposure times are completely consistent with predicted survey progress based on target magnitude and colour.

An example spectrum of a faint source and a selection of corresponding multiband images can be seen in Fig. 19. This source sits at the faint end of our sample (Y = 21.18 mag) and took the combination of 3× ∼ 1-h exposures to obtain a secure redshift. As part of the TAZ pipeline, we produce similar diagnostic plots for all spectra in the DEVILS sample. As a series of other examples, we include similar plots for a faint (Y = 21.12 mag) absorption line system, bright (Y = 19.25 mag) emission line system, and bright (Y = 19.38 mag) absorption line system in Appendix A.

To highlight our current survey progress, Fig. 20 displays the target density (left), pre-DEVILS completeness to Y < 21.2 mag (middle), and currently completeness including DEVILS redshifts (right) in the D03 and D10 fields gridded in 2 arcmin bins – D02 was not observed in 2017B. Within D03, we have already significantly increased the completeness over the entire region, while in D10, we have made significant progress in filling in the non-uniformity in completeness produced (predominantly) by the zCOSMOS footprint. DEVILS has already increased the median completeness to our Y < 21.2 mag limit in 2 × 2 arcmin bins and has increased from 25 per cent to 38 per cent in D03 and 54 per cent to 67 per cent in D10 (for mean completeness: 26 per cent to 39 per cent in D03 and 54 per cent to 64 per cent in D10).

At the time DEVILS was observing the D03 field, the Dark Energy Survey (Flaugher 2005) was also discovering transient sources in this field using DECam on the CTIO 4m telescope. As part of our fibre exchange with OzDES, a number of 2dF fibres were allocated to these transients in the D03 region during the December and January runs. 22 transients were observed, obtaining redshifts for 18 and classifying six of them as supernovae (these will be presented in two upcoming ATEL publications).

In addition to the transients, 55 AGN from the OzDES reverberation mapping program were also observed during the January run. This program has been running since 2013, and the additional observations undertaken by DEVILS increases the number of points that

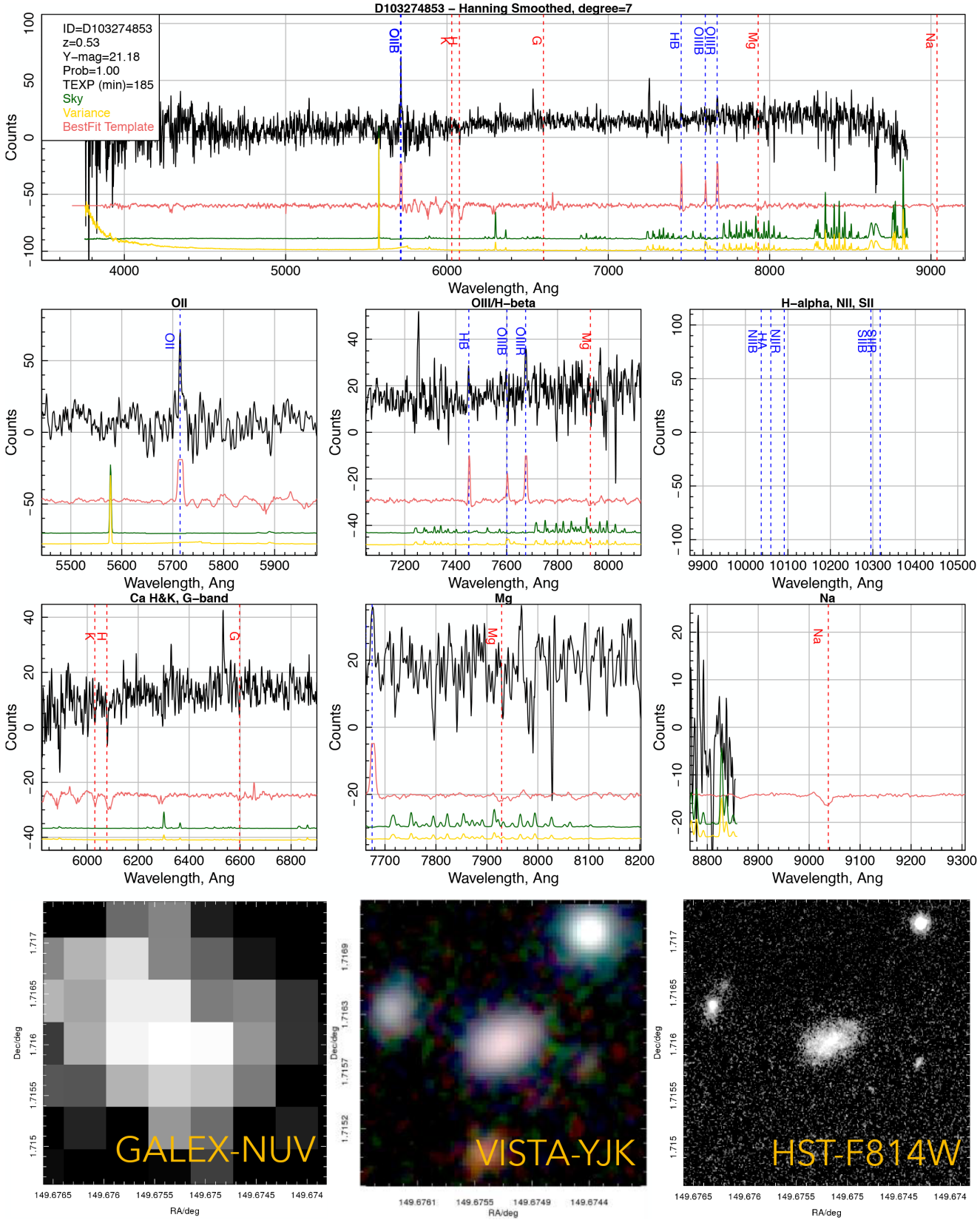

Figure 19. Example spectrum of source D103274853 in the D10 region. The top row shows the full spectrum, middle rows key regions of emission (top) and absorption (bottom) line, and bottom row GALEX, VISTA, and *HST* imaging for this source. Note that H α and Na fall outside of the spectral range for this source. The galaxy has faintly detected OII, H β, and OIII emission lines and Ca H&K absorption feature. The target had its redshift correctly identified by AUTOZ (Baldry et al. 2014) in just over 3-h integration with a probability of 1 (very secure). Key source parameters are given in the legend but rounded to two decimal places for ease of plotting. Overplotted are the variance and sky spectrum from the stacked AAT observation, as well as the best-fitting template from AUTOZ.

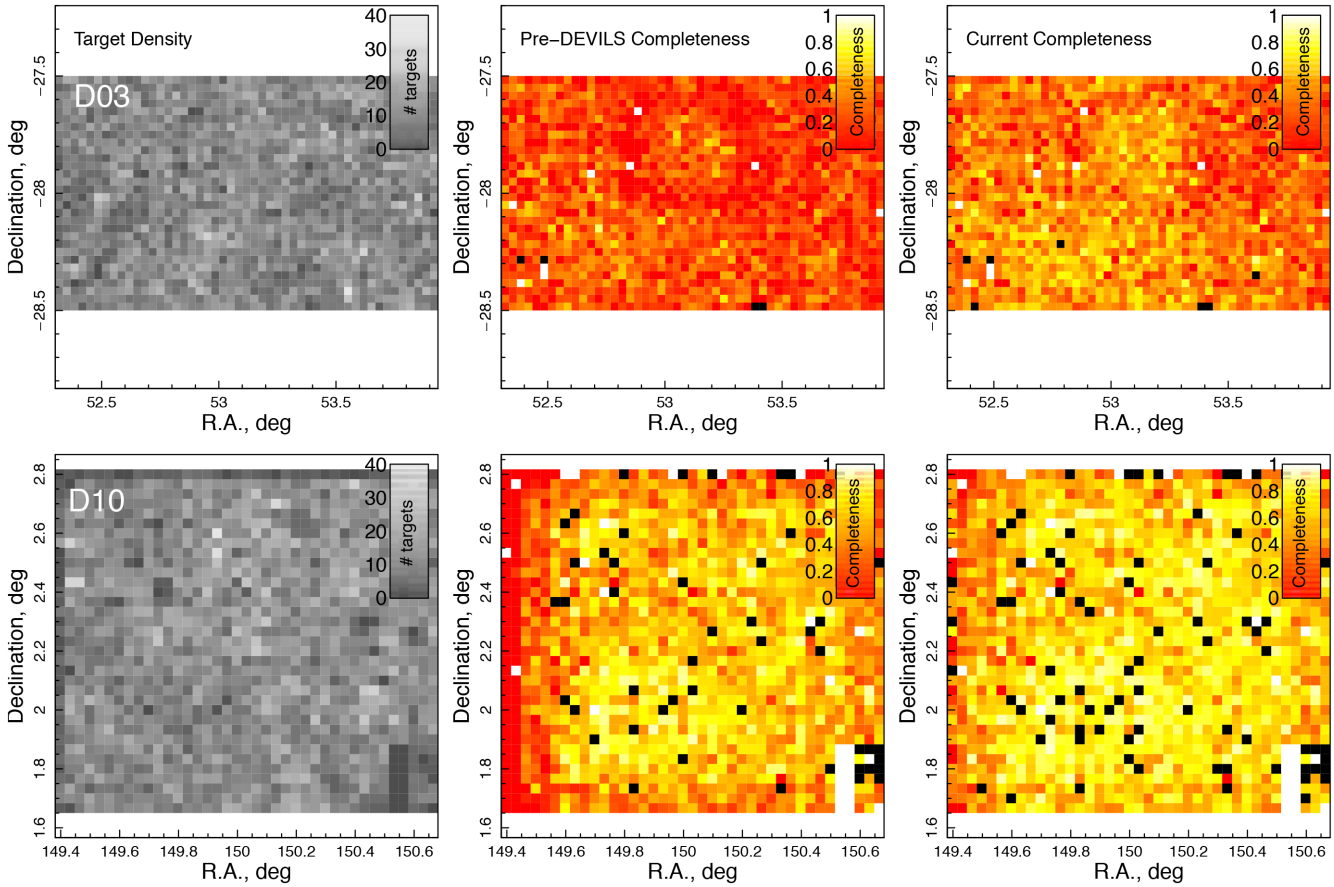

Figure 20. The pre-DEVILS and post-2017B observations completeness to $Y < 21.2$ mag targets in D03 (top) and D10 (bottom) – gridded in 2×2 arcmin bins. Left: $Y < 21.2$ mag source density, middle: the pre-DEVILS redshift completeness, right: the current redshift completeness. Bins with > 95 per cent completeness are shown in black.

can be used and therefore increases the likelihood of a successful AGN-lag measurement.

6.5 Planned public data releases

The DEVILS survey has a number of planned public data releases both in terms of AAT spectroscopy and associated multiwavelength imaging with consistent processing and derived properties. These data will be hosted and made public via AAO Data Central[8] once the core science of the project has been completed. It is currently expected that our initial data release containing spectra from the D10 region will occur in 2020 with subsequent full data release in 2022. However, this is subject to change based on time allocation and completion of core science projects. The preliminary (DR0) DEVILS input catalogue and a cutout service for imaging in the D10 region (covering imaging data from X-ray to far-IR wavelengths) are currently available through this service.

7 SUMMARY

The DEVILS is a spectroscopic campaign at the AAT aimed at bridging the near and distant Universe by producing the highest completeness survey of galaxies and groups at intermediate redshifts ($0.3 < z < 1.0$). The key science aims of the survey are to measure the late time evolution of the high-mass end of the HMF (as predicted by ΛCDM) and the effect of environment in regulating galaxy evolution of the last eight billion years. A summary overview of our key science goals is presented in Section 2.

Using the PROFOUND source-finding code and UltraVISTA/VIDEO imaging, we have selected a sample of 57 000 $Y < 21.2$ mag galaxies over $\sim$6 deg^2 in three well-studied deep extragalactic fields (COSMOS, XMM-LSS, and ECDFS, see Section 4 for our photometric selection). Within this process, we perform robust star–galaxy separation (Section 4.5), masking of artefact regions (Section 4.7), and visual classifications (Section 4.6). We form a final target list of sources that do not currently have a secure redshift in our sample and discuss our AAT-observing strategy for obtaining redshifts for these sources. As part of this process, we have developed a nightly redshift-feedback mechanism to maximize survey efficiency, allowing sources to be observed for the minimum time required to obtain a redshift (Section 6.2). DEVILS observations began in late 2017 (Section 6.4) and we have currently obtained 4353 new redshifts. Strategies such as these will be essential for the next generation of large spectroscopic surveys, i.e. the Wide Area VISTA Extragalactic Survey (WAVES, Driver et al. 2016c). DEVILS observations will continue until 2021–22, with planned data releases via AAO Data Central.

[8] https://datacentral.aao.gov.au

ACKNOWLEDGEMENTS

DEVILS is an Australian project based around a spectroscopic campaign using the *Anglo-Australian Telescope*. The DEVILS input catalogue is generated from data taken as part of the ESO VISTA-VIDEO (Jarvis et al. 2013) and UltraVISTA (McCracken et al. 2012) surveys. DEVILS is partly funded via Discovery Programs by the Australian Research Council and the participating institutions. The DEVILS website is https://devilsurvey.org. The DEVILS data are hosted and provided by AAO Data Central (datacentral.aao.gov.au). Parts of this research were conducted by the Australian Research Council Centre of Excellence for All Sky Astrophysics in 3 Dimensions (ASTRO 3D) through project number CE170100013.

REFERENCES

AAO software Team, 2015, ascl.soft, ascl:1505.015
Abazajian K. N. et al., 2009, ApJS, 182, 543
Aihara H. et al., 2017, PASJ, 70S, 8A
Alpaslan M. et al., 2014, MNRAS, 438, 177
Alpaslan M. et al., 2015, MNRAS, 451, 3249
Andrews S. K., Driver S. P., Davies L. J. M., Kafle P. R., Robotham A. S. G., Wright A. H., 2017, MNRAS, 464, 1569
Aretxaga I. et al., 2011, MNRAS, 415, 3831
Atek H. et al., 2011, ApJ, 743, 121
Baldry I. K. et al., 2010, MNRAS, 404, 86
Baldry I. K. et al., 2012, MNRAS, 421, 621
Baldry I. K. et al., 2014, MNRAS, 441, 2440
Baugh C. M., 2006, RPPh, 69, 3101
Behroozi P. S., Wechsler R. H., Conroy C., 2013, ApJ, 770, 57
Bell E. F., de Jong R. S., 2000, MNRAS, 312, 497
Bell E. F., McIntosh D. H., Katz N., Weinberg M. D., 2003, ApJS, 149, 289
Bell E. F. et al., 2005, ApJ, 625, 23
Bell E. F. et al., 2006, ApJ, 640, 241
Belli S., Newman A. B., Ellis R. S., 2017, ApJ, 834, 18
Bennett C. L. et al., 2013, ApJS, 208, 20
Bernyk M. et al., 2016, ApJS, 223, 9
Bertin E., Arnouts S., 1996, A&AS, 117, 393
Bigiel F., Leroy A., Walter F., Brinks E., de Blok W. J. G., Madore B., Thornley M. D., 2008, AJ, 136, 2846
Blake C. et al., 2016, MNRAS, 462, 4240
Bolzonella M. et al., 2010, A&A, 524, A76
Brown T. et al., 2017, MNRAS, 466, 1275
Bruzual G., Charlot S., 2003, MNRAS, 344, 1000
Bryant J. J. et al., 2015, MNRAS, 447, 2857
Bundy K., Fukugita M., Ellis R. S., Kodama T., Conselice C. J., 2004, ApJ, 601, L123
Bundy K., Fukugita M., Ellis R. S., Targett T. A., Belli S., Kodama T., 2009, ApJ, 697, 1369
Caldwell C. E., McCarthy I. G., Baldry I. K., Collins C. A., Schaye J., Bird S., 2016, MNRAS, 462, 4117
Calzetti D., Kinney A. L., Storchi-Bergmann T., 1994, ApJ, 429, 582
Cappellari M. et al., 2011, MNRAS, 416, 1680
Cappelluti N. et al., 2009, A&A, 497, 635
Chabrier G., 2003, PASP, 115, 763
Chang Y.-Y., van der Wel A., da Cunha E., Rix H.-W., 2015, ApJS, 219, 8
Chen C-T J, et al., 2018, MNRAS, 478, 2132
Childress M. J. et al., 2017, MNRAS, 472, 273
Codis S., Pichon C., Pogosyan D., 2015, MNRAS, 452, 3369
Cohen M., Wheaton W. A., Megeath S. T., 2003, AJ, 126, 1090
Colless M. et al., 2001, MNRAS, 328, 1039
Conselice C. J., 2014, ARA&A, 52, 291
Cooper M. C. et al., 2012, MNRAS, 419, 3018
Cortese L., Catinella B., Boissier S., Boselli A., Heinis S., 2011, MNRAS, 415, 1797
Croom S., Saunders W., Heald R., 2004, AAONw, 106, 12
Croton D. J. et al., 2016, ApJS, 222, 22
da Cunha E. et al., 2017, PASA, 34, e047
Damjanov I., Zahid H. J., Geller M. J., Fabricant D. G., Hwang H. S., 2018, ApJS, 234, 21
Darvish B., Mobasher B., Sobral D., Hemmati S., Nayyeri H., Shivaei I., 2015, ApJ, 814, 84
Darvish B., Mobasher B., Sobral D., Rettura A., Scoville N., Faisst A., Capak P., 2016, ApJ, 825, 113
Davidzon I. et al., 2016, A&A, 586, A23
Davies L. J. M. et al., 2015a, MNRAS, 447, 1014
Davies L. J. M. et al., 2015b, MNRAS, 452, 616
Davies L. J. M. et al., 2016a, MNRAS, 455, 4013
Davies L. J. M. et al., 2016b, MNRAS, 461, 458
de Jong J. T. A., Verdoes Kleijn G. A., Kuijken K. H., Valentijn E. A., 2013, Exp. Astron., 35, 25
de Jong R. S. et al., 2014, SPIE, 9147, 91470M
de Ravel L. et al., 2009, A&A, 498, 379
Dressler A., 1980, ApJ, 236, 351
Drinkwater M. J. et al., 2018, MNRAS, 474, 4151
Driver S. P., Davies L. J., Meyer M., Power C., Robotham A. S. G., Baldry I. K., Liske J., Norberg P., 2016c, ASSP, 42, 205
Driver S. P., Robotham A. S. G., 2010, MNRAS, 407, 2131
Driver S. P. et al., 2011, MNRAS, 413, 971
Driver S. P. et al., 2016a, ApJ, 827, 108
Driver S. P. et al., 2016v, MNRAS, 455, 3911
Driver S. P. et al., 2018, MNRAS, 475, 2891
Eales S. et al., 2015, MNRAS, 452, 3489
Eardley E. et al., 2015, MNRAS, 448, 3665
Eke V. R., Baugh C. M., Cole S., Frenk C. S., Navarro J. F., 2006, MNRAS, 370, 1147
Elahi P. J., Welker C., Power C., del P Lagos C., Robotham A. S. G., Cañas R., Poulton R., 2018, MNRAS, 475, 5338E
Elbaz D. et al., 2007, A&A, 468, 33
Fabian A. C., 2012, ARA&A, 50, 455
Fernández X. et al., 2013, ApJ, 770, L29
Flaugher B., 2005, IJMPA, 20, 3121
Fogarty L. M. R. et al., 2014, MNRAS, 443, 485
Garilli B. et al., 2014, A&A, 562, A23
Geller M. J., Hwang H. S., Dell'Antonio I. P., Zahid H. J., Kurtz M. J., Fabricant D. G., 2016, ApJS, 224, 11
Giovanelli R., Haynes M. P., 1985, ApJ, 292, 404
Girardi L., Groenewegen M. A. T., Hatziminaoglou E., da Costa L., 2005, A&A, 436, 895
Grootes M. W. et al., 2017, AJ, 153, 111
Gunn J. E., Gott J. R., III, 1972, ApJ, 176, 1
Hatfield P. W., Lindsay S. N., Jarvis M. J., Häußler B., Vaccari M., Verma A., 2016, MNRAS, 459, 2618
Haynes D. M. et al., 2016, SPIE, 9908, 99088I
Holwerda B. W., Blyth S., Baker A. J., MeerKAT Deep HI Survey Team, 2011, AAS, 43, 433.17
Hopkins A. M., Beacom J. F., 2006, ApJ, 651, 142
Hopkins P. F., Cox T. J., Kereš D., Hernquist L., 2008, ApJS, 175, 390
Huynh M. T., Hopkins A. M., Lenc E., Mao M. Y., Middelberg E., Norris R. P., Randall K. E., 2012, MNRAS, 426, 2342
Jarvis M. J. et al., 2013, MNRAS, 428, 1281
Jarvis M. J. et al., 2017, preprint (arXiv:1709.01901)
Jogee S. et al., 2009, ApJ, 697, 1971
Kafle P. R., Robotham A. S. G., Driver S. P., Deeley S., Norberg P., Drinkwater M. J., Davies L. J., 2018, preprint (arXiv:1802.09009)
Kartaltepe J. S. et al., 2007, ApJS, 172, 320
Kauffmann G., Heckman T. M., De Lucia G., Brinchmann J., Charlot S., Tremonti C., White S. D. M., Brinkmann J., 2006, MNRAS, 367, 1394
Kauffmann G., White S. D. M., Heckman T. M., Ménard B., Brinchmann J., Charlot S., Tremonti C., Brinkmann J., 2004, MNRAS, 353, 713
Kennicutt R. C., Evans N. J., 2012, ARA&A, 50, 531
Knobel C. et al., 2012, ApJ, 753, 121
Kochanek C. S. et al., 2012, ApJS, 200, 8

Kodama T., Smail I., Nakata F., Okamura S., Bower R. G., 2001, ApJ, 562, L9
Kormendy J., Ho L. C., 2013, ARA&A, 51, 511
Kraljic K. et al., 2018, MNRAS, 474, 547
Kron R. G., 1980, ApJS, 43, 305
Lacey C. G. et al., 2016, MNRAS, 462, 3854
Lagos C. d. P. et al., 2018, MNRAS, 473, 4956
Lah P. et al., 2007, MNRAS, 376, 1357
Laigle C. et al., 2016, ApJS, 224, 24
Lange R. et al., 2015, MNRAS, 447, 2603
Larson R. B., Tinsley B. M., Caldwell C. N., 1980, ApJ, 237, 692
Laureijs R. et al., 2011, preprint (arXiv:1110.3193)
Leauthaud A. et al., 2012, ApJ, 744, 159
Lee N. et al., 2015, ApJ, 801, 80
Le Fèvre O. et al., 2013, A&A, 559, A14
Le Fèvre O. et al., 2014, Msngr, 155, 37
Le Fèvre O. et al., 2015, A&A, 576, A79
Lewis I. J. et al., 2002, MNRAS, 333, 279
Lilly S. J. et al., 2007, ApJS, 172, 70
Lin L. et al., 2016, ApJ, 817, 97
Liske J. et al., 2015, MNRAS, 452, 2087
Lonsdale C. J. et al., 2003, PASP, 115, 897
Lotz J. M., Jonsson P., Cox T. J., Croton D., Primack J. R., Somerville R. S., Stewart K., 2011, ApJ, 742, 103
Madau P., Dickinson M., 2014, ARA&A, 52, 415
Marchesini D., van Dokkum P. G., Förster Schreiber N. M., Franx M., Labbé I., Wuyts S., 2009, ApJ, 701, 1765
Mauduit J.-C. et al., 2012, PASP, 124, 714
McConnachie A. et al., 2016, preprint (arXiv:1606.00043)
McCracken H. J. et al., 2012, A&A, 544, A156
McNaught-Roberts T. et al., 2014, MNRAS, 445, 2125
Miller N. A. et al., 2013, ApJS, 205, 13
Moffett A. J. et al., 2016, MNRAS, 462, 4336
Moore B., Lake G., Quinn T., Stadel J., 1999, MNRAS, 304, 465
Murray S. G., Power C., Robotham A. S. G., 2013, MNRAS, 434, L61
Muzzin A. et al., 2013, ApJ, 777, 18
Newman J. A. et al., 2013, ApJS, 208, 5
Nichols M., Bland-Hawthorn J., 2011, ApJ, 732, 17
Nichols M., Bland-Hawthorn J., 2013, ApJ, 775, 97
Norris R. P. et al., 2006, AJ, 132, 2409
Oliver S. J. et al., 2012, MNRAS, 424, 1614
Ostriker J. P., Tremaine S. D., 1975, ApJ, 202, L113
Pacaud F. et al., 2016, A&A, 592, A2
Panter B., Heavens A. F., Jimenez R., 2004, MNRAS, 355, 764
Patton D. R., Ellison S. L., Simard L., McConnachie A. W., Mendel J. T., 2011, MNRAS, 412, 591
Peacock J. A. et al., 2001, Nature, 410, 169
Peng Y.-j. et al., 2010, ApJ, 721, 193
Pierre M. et al., 2004, JCAP, 9, 011
Pierre M. et al., 2006, MNRAS, 372, 591
Planck Collaboration I, 2016, A&A, 594, A1
Poggianti B. M. et al., 2017, ApJ, 844, 48
Popesso P. et al., 2011, A&A, 534, C2
Popesso P. et al., 2012, A&A, 537, A58
Popping G., Somerville R. S., Trager S. C., 2014, MNRAS, 442, 2398
Press W. H., Schechter P., 1974, ApJ, 187, 425
Ranalli P. et al., 2013, A&A, 555, A42
Rhee J., Lah P., Briggs F. H., Chengalur J. N., Colless M., Willner S. P., Ashby M. L. N., Le Fèvre O., 2018, MNRAS, 473, 1879
Rhee J., Lah P., Chengalur J. N., Briggs F. H., Colless M., 2016, MNRAS, 460, 2675
Rix H.-W., et al., 2004, ApJS, 152, 163
Robaina A. R. et al., 2009, ApJ, 704, 324
Robotham A. et al., 2010, PASA, 27, 76
Robotham A. S. G, Davies L. J. M., Driver S. P., Koushan S., Taranu D. S., Casura S., Liske J., 2018, MNRAS, 476, 3137
Robotham A. S. G. et al., 2011, MNRAS, 416, 2640
Robotham A. S. G. et al., 2014, MNRAS, 444, 3986
Sancisi R., Fraternali F., Oosterloo T., van der Hulst T., 2008, A&ARv, 15, 189
Sanders D. B. et al., 2007, ApJS, 172, 86
Saunders W. et al., 2004, Proc. SPIE, 5492, 389
Schaye J. et al., 2010, MNRAS, 402, 1536
Schaye J. et al., 2015, MNRAS, 446, 521
Schinnerer E. et al., 2007, ApJS, 172, 46
Scoville N. et al., 2007, ApJS, 172, 1
Scudder J. M., Ellison S. L., Momjian E., Rosenberg J. L., Torrey P., Patton D. R., Fertig D., Mendel J. T., 2015, MNRAS, 449, 3719
Scudder J. M., Ellison S. L., Torrey P., Patton D. R., Mendel J. T., 2012, MNRAS, 426, 549
Sharp R. et al., 2006, Proc. SPIE, 6269, 62690G
Smith G. P., Treu T., Ellis R. S., Moran S. M., Dressler A., 2005, ApJ, 620, 78
Smolčić V. et al., 2014, MNRAS, 443, 2590
Smolčić V. et al., 2017, A&A, 602, A1
Springel V. et al., 2005, Nature, 435, 629
Surace J. A. et al., 2004, yCat, 2255
Tanaka M. et al., 2017, preprint (arXiv:1706.00566)
Taniguchi Y. et al., 2015, PASJ, 67, 104
Tasse C., Röttgering H. J. A., Best P. N., Cohen A. S., Pierre M., Wilman R., 2007, A&A, 471, 1105
Tasse C. et al., 2006, A&A, 456, 791
Taylor E. N. et al., 2011, MNRAS, 418, 1587
Tomczak A. R. et al., 2014, ApJ, 783, 85
Tomczak A. R. et al., 2017, MNRAS, 472, 3512
Vaccari M. et al., 2016, heas.conf, 26,
van der Wel A. et al., 2012, ApJS, 203, 24
van der Wel A. et al., 2016, ApJS, 223, 29
Verheijen M., van Gorkom J. H., Szomoru A., Dwarakanath K. S., Poggianti B. M., Schiminovich D., 2007, ApJ, 668, L9
Vikhlinin A. et al., 2009, ApJ, 692, 1060
Viola M. et al., 2015, MNRAS, 452, 3529
Virani S. N., Treister E., Urry C. M., Gawiser E., 2006, AJ, 131, 2373
Vulcani B. et al., 2013, A&A, 550, A58
White S. D. M., Rees M. J., 1978, MNRAS, 183, 341
Windhorst R. A. et al., 2011, ApJS, 193, 27
Wolf C., Dye S., Kleinheinrich M., Meisenheimer K., Rix H.-W., Wisotzki L., 2001, A&A, 377, 442
Wolf C. et al., 2004, A&A, 421, 913
Wong T., Blitz L., 2002, ApJ, 569, 157
Wright A. H. et al., 2016, MNRAS, 460, 765
Wright A. H. et al., 2017, MNRAS, 470, 283
Xu C. K. et al., 2005, ApJ, 619, L11
Yang X., Mo H. J., van den Bosch F. C., 2009, ApJ, 695, 900
Yang X., Mo H. J., van den Bosch F. C., Pasquali A., Li C., Barden M., 2007, ApJ, 671, 153
Yuan F. et al., 2015, MNRAS, 452, 3047
Zamojski M. A. et al., 2007, ApJS, 172, 468
Ziparo F. et al., 2014, MNRAS, 437, 458

APPENDIX A: OTHER EXAMPLES OF 2017B SPECTRA

This appendix provides further examples of the spectra obtained in our 2017B observations for different galaxy type. We include faint ($Y = 21.12$ mag) absorption line system at $z \sim 0.34$ A1, a bright ($Y = 19.25$ mag) emission line system at $z \sim 0.21$ A2, and a bright ($Y = 19.38$ mag) absorption line system at $z \sim 0.53$ A3.

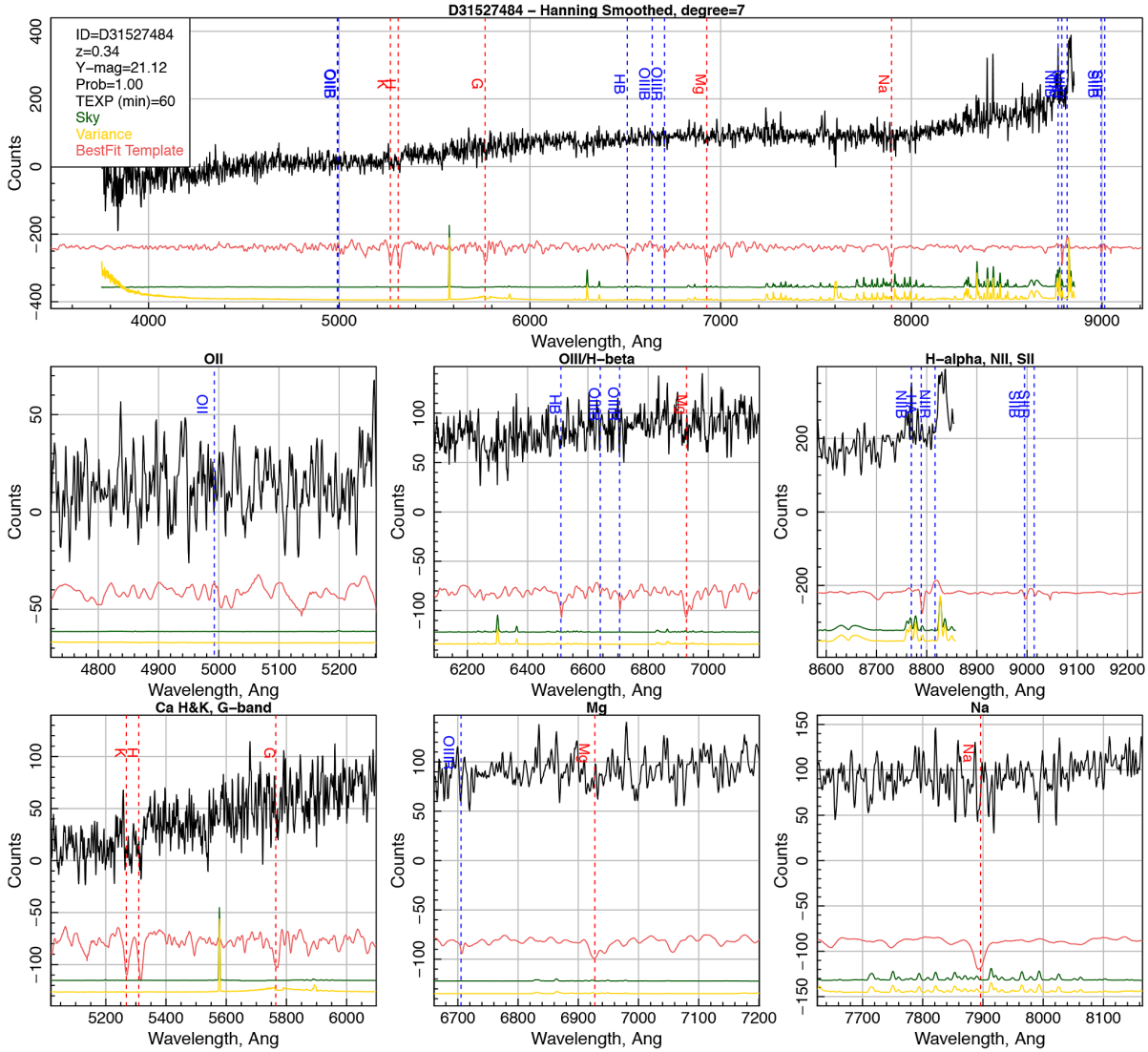

Figure A1. The same as Fig. 19 but for a faint ($Y = 21.12$ mag) absorption line system at $z \sim 0.34$.

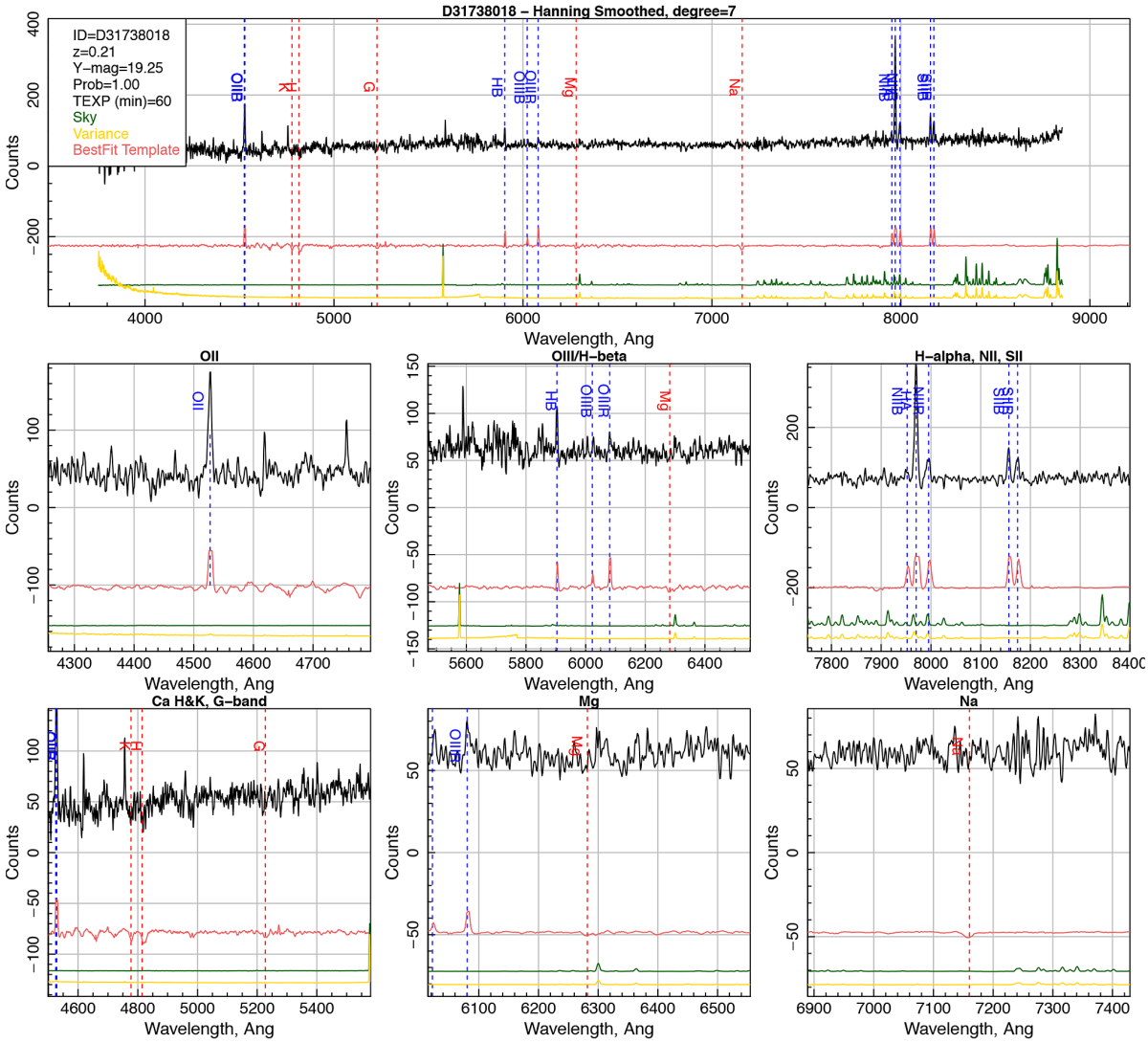

Figure A2. The same as Fig. 19 but for a bright ($Y = 19.25$ mag) emission line system at $z \sim 0.21$.

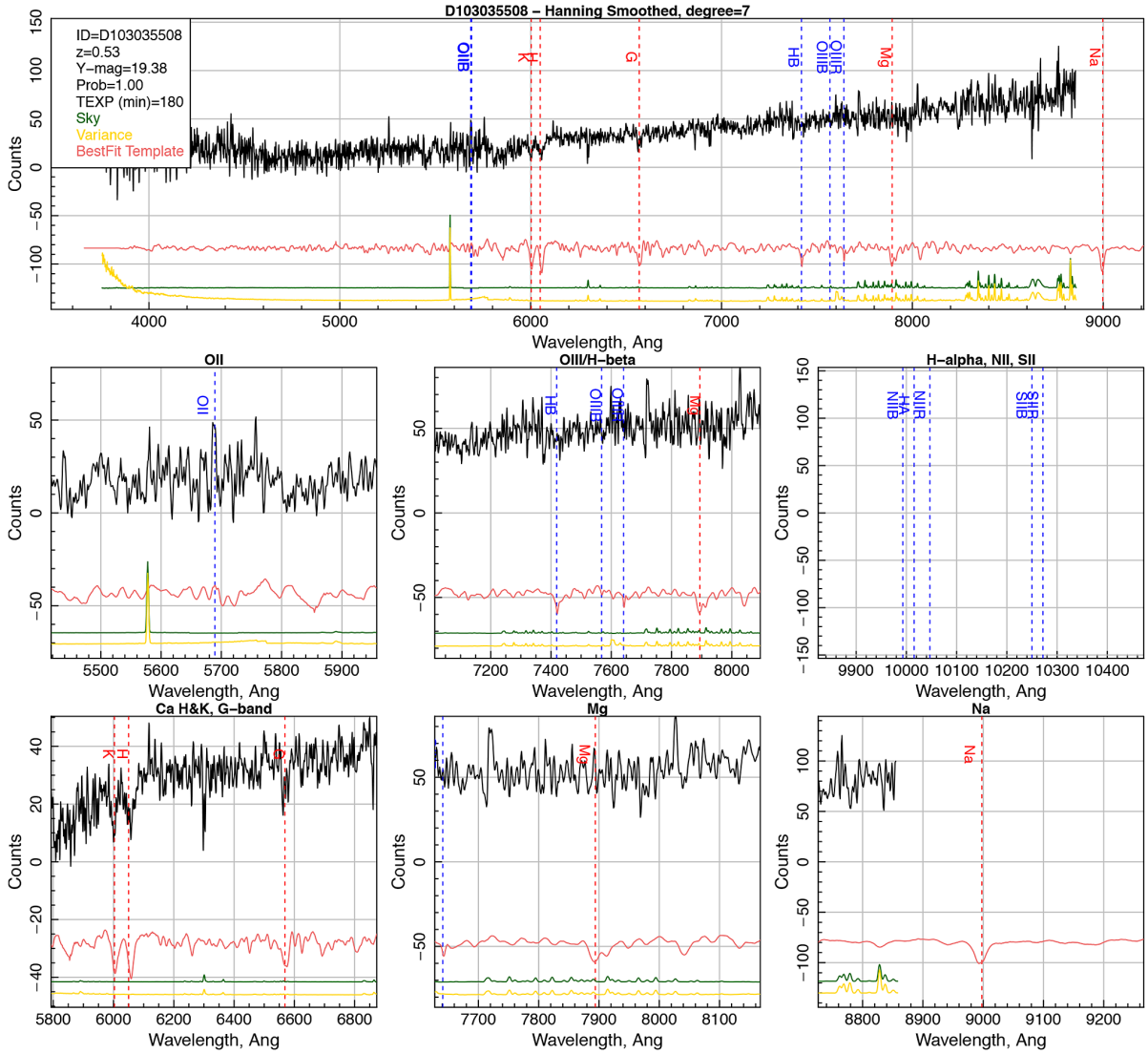

Figure A3. The same as Fig. 19 but for a bright ($Y = 19.38$ mag) absorption line system at $z \sim 0.53$.

[1]*ICRAR, The University of Western Australia, 35 Stirling Highway, Crawley, WA 6009, Australia*
[2]*Australian Research Council Centre of Excellence for All-sky Astrophysics (CAASTRO), 44 Rosehill Street Redfern, NSW 2016, Australia*
[3]*Australian Astronomical Observatory, 105 Delhi Rd, North Ryde, NSW 2113, Australia*
[4]*Sydney Institute for Astronomy, School of Physics, A28, The University of Sydney, NSW 2006, Australia*
[5]*Australian Research Council Centre of Excellence for All Sky Astrophysics in 3 Dimensions (ASTRO 3D)*
[6]*Research School of Astronomy and Astrophysics, Australian National University, Canberra, ACT 2611, Australia*
[7]*Astrophysics Research Institute, Liverpool John Moores University, IC2, Liverpool Science Park, 146 Brownlow Hill, Liverpool L35RF, UK*
[8]*Leiden Observatory, Leiden University, Niels Bohrweg 2, NL-2333 CA Leiden, the Netherlands*
[9]*National Centre for Nuclear Research, Astrophysics Division, PO Box 447, PL-90-950 Lodz, Poland*
[10]*HH Wills Physics Laboratory, University of Bristol, Tyndall Avenue, Bristol BS8 1TL, UK*
[11]*School of Physics and Astronomy, Monash University, Clayton, VIC 3800, Australia*
[12]*ESA/ESTEC SCI-S, Keplerlaan 1, 2201 AZ Noordwijk, the Netherlands*
[13]*Department of Physics and Astronomy, 102 Natural Science Building, University of Louisville, Louisville KY 40292, USA*
[14]*Oxford Astrophysics, Department of Physics, Keble Road, Oxford OX1 3RH, UK*
[15]*Department of Physics, University of the Western Cape, Bellville 7535, South Africa*
[16]*ASTRON, the Netherlands Institute for Radio Astronomy, Postbus 2, 7990 AA, Dwingeloo, the Netherlands*
[17]*Vanderbilt University, Department of Physics and Astronomy, Nashville, TN 37240, USA*
[18]*Centre for Astrophysics and Supercomputing, Swinburne University of Technology, Hawthorn 3122, Australia*
[19]*School of Earth & Space Exploration, Arizona State University, PO Box 871404, Tempe, AZ 85287, USA*

This paper has been typeset from a TEX/LATEX file prepared by the author.